Journal of Non-Newtonian Fluid Mechanics 295 (2021) 104617

Contents lists available at ScienceDirect

Journal of Non-Newtonian Fluid Mechanics

journal homepage: www.elsevier.com/locate/jnnfm

Polyelectrolyte solutions in Taylor-Couette flows

Vishal Panwar [a,1], Athena E. Metaxas [b,1], Cari S. Dutcher [a,b,*]

[a] Department of Mechanical Engineering, University of Minnesota–Twin Cities, 111 Church Street SE, Minneapolis, MN, 55455, USA
[b] Department of Chemical Engineering and Materials Science, University of Minnesota–Twin Cities, 421 Washington Avenue SE, Minneapolis, MN, 55455, USA

ARTICLE INFO

Key words:
Taylor-Couette flow
Polymer solutions
Polyelectrolytes

ABSTRACT

Taylor-Couette (TC) flow is ideal for studying the flow behavior of complex solutions due to the wide variety of available hydrodynamic flow states. For non-Newtonian solutions, the presence of polymers in solution changes the solution rheology, which in turn modifies accessible flow states. While significant prior work exists on the effects of elasticity and shear thinning of polymer solutions on TC flow, the effects of changes in polymer chain conformation on these properties and the resultant changes in the TC flow states have not been extensively studied. Here, we have explored the effects of changing polymer chain conformation of polyelectrolyte solutions on laminar and turbulent TC flow by using a quasi-static ramp protocol to vary the inner cylinder rotation rates. The ionic strength of the cationic polyacrylamide (CPAM) solution was varied to modify the equilibrium polymer equilibrium conformation and solution rheological properties. In general, as the increasing solution ionic strength increases polymer chain flexibility and decreases elasticity and degree of shear thinning, there is a shift toward more Newtonian-like flow behavior. Additionally, the effects of co- and counter-rotation of the cylinders on the stability of flow states were observed as a function of solution ionic strength, and phase diagrams of the resulting flow states were mapped as a function of the inner and outer cylinder Reynolds numbers. It was found that co-rotation of the cylinders stabilizes some of the polymer-influenced flow states, while counter-rotation destabilizes flow states.

1. Introduction

1.1. Taylor-Couette flows

The study of Taylor-Couette (TC) flow, or azimuthal flow between two concentric rotating cylinders, has been and continues to be a topic of interest due to the significant insights it provides for the study of flow properties and hydrodynamics. Because the inner and outer cylinders can be independently rotated, a wide variety of hydrodynamic flow conditions becomes accessible. TC flow dynamics are characterized by the Reynolds number (*Re*) for both the inner (*in*) and outer (*out*) cylinders, defined by

$$Re_{in,out} = \Omega_{in,out} R_{in,out} d/\nu, \tag{1}$$

where Ω refers to the cylinder rotation speed, R is the cylinder radius, d is the width of the annulus, or gap, between the two cylinders ($d = R_{out} - R_{in}$), and ν is the kinematic viscosity of the fluid enclosed within the annulus. When discussing the flow states accessible by TC cells, one must also note the geometric parameters of the radius ratio and the aspect ratio in addition to the dynamic parameter of *Re*. The radius ratio, η, is defined as $\eta = R_{in}/R_{out}$. The relative range of fluid streamline curvature is encapsulated in the radius ratio and for this study is fixed in the narrow gap regime [1]. The aspect ratio, Γ, is defined as $\Gamma = h/d$, where h is the height of the cylinder. To avoid end effects, the aspect ratio in this study is in the large aspect ratio regime [2].

Over the past century, an extensive amount of work has been conducted to study narrow gap, large aspect ratio TC flows, from the seminal study by Taylor [3], followed by Coles [4], Snyder [5], Walsh and Donnelly [6], Jones [7], and Andereck, Liu, and Swinney [8], among many others. A variety of flow conditions has been found for Newtonian solutions, starting from circular Couette flow. As the Reynolds number for the inner cylinder increases, the flow transitions at a critical point to toroidal vortices (Taylor vortex flow, TVF). Further increasing the angular speed, and therefore the Reynolds number, introduces oscillations into the flow (wavy vortex flow, WVF). As the Reynolds number continues increasing, the flow eventually becomes turbulent, and turbulent wavy vortex flow (TWV) and turbulent Taylor vortex flow (TTV) are achieved [9]. These are only a few of the many flow states that are

* Corresponding author.
E-mail address: cdutcher@umn.edu (C.S. Dutcher).
[1] indicates equal author contribution

https://doi.org/10.1016/j.jnnfm.2021.104617
Received 9 April 2021; Received in revised form 12 July 2021; Accepted 13 July 2021
Available online 18 July 2021

accessible by Taylor-Couette cells, where factors such as co- and counter-rotation of the inner cylinder with respect to the outer cylinder and fluid type can access additional flow types [10,11].

1.2. Non-Newtonian considerations for TC flow

Since non-Newtonian solution dynamics are dependent on the material properties of a fluid, relatively subtle differences in these rheological properties (*i.e.,* shear-rate dependent solution viscosity, relaxation time, normal stress coefficients, elasticity, chain stiffness, *etc.*) can lead to significant stability changes and shifted flow state transitions in TC flow. Many studies exist that have explored the effects on TC flow from changes in shear thinning properties of solutions. Experimental studies have shown that an increase in shear thinning decreases the critical *Re* for the initial transition to Taylor vortex flow, Re_{cr} [12–14]. In these studies, the degree of shear thinning is primarily modified through changes in the polymer concentration, with attention paid to whether the concentration was in the dilute or semi-dilute regime. The experimental findings have been further corroborated by numerical predictions. Ashraf et al. [15] looked at the stability analysis of shear thinning fluids in a TC cell, where it was observed that shear thinning property of the fluid lowers the critical Taylor number for transition from base flow to a vortex structure, and the practical difficulty to isolate effects of shear thinning from elasticity was noted. Lockett et al. [16] used finite-element techniques to find that shear thinning had significant effects on critical Taylor number and critical wavenumber. Khali et al. [17] used the lattice Boltzmann method to study the instability for both Newtonian and non-Newtonian fluids numerically, with two flow modes: Couette flow (CF) and secondary TVF mode. The critical Reynolds number was found to be a monotonic increase with the power-law index, *n*, of the non-Newtonian fluid. Finally, Thomas et al. [18] simulated viscoelastic Taylor Couette flows of dilute polymer solutions using a fully implicit parallel spectral time-splitting algorithm and studied flow patterns such as rotating standing waves (RSWs), disordered oscillations (DOs), oscillatory strips (OSs), and diwhirls (DWs). In general, the flow instabilities were dynamically simulated for varying degrees of elasticity. However, even for the known Weissenberg numbers (defined as the ratio of elastic to viscous forces), the flow transition boundaries to disordered states remain unknown and would require further experiments with properly characterized fluids. A combined theoretical and experimental effort was suggested for a better understanding.

A fair amount of study has also been conducted through changing the elasticity of non-Newtonian fluids in Taylor-Couette flow. Earlier studies examined how dilute, weakly elastic polymer solutions affect the stability of TC flow, where critical flow transitions occurred earlier or later than their Newtonian counterparts, while others have explored the inertial and inertial-elastic instabilities in the flow [19–25]. Several studies observed the effects of fluid properties such as elasticity on flow stability, where additional flow types such as helical and non-axisymmetric standing waves were observed [26–28]. Dutcher and Muller [29,30] have explored the effects of weak and moderate elasticity on the stability of high Reynolds number TC flow, where the sequence to the turbulent transition was modified by increasing the elasticity of the fluid. Indeed, a sufficiently elastic polymer solution can induce a form of turbulence known as “elastic turbulence” that occurs at *Re* values well below values typically associated with turbulence [31,32]. Elastic effects are quantified by the elasticity number, *El*, which is the ratio of elastic to inertial forces and can be quantified by Eq. 2, where λ_E is the longest relaxation time of the polymer. In this study, the longest relaxation time corresponded to the extensional relaxation time of the polymer solution as measured by Capillary Breakup Extensional Rheometry (CaBER).

$$El = \lambda_E \nu / d^2 \tag{2}$$

For highly elastic polymer solutions, a purely elastic instability is governed by the Deborah number, *De,* which is defined as the ratio of solution relaxation time to residence time in the flow, and is characterized by isolated vortex pairs called ‘diwhirls’ [33–38].

Like the flow behavior index, which quantifies the extent of shear thinning, the elasticity number is modified in most studies through changes in polymer molecular weight, solvent viscosity, or polymer concentration. Less information exists on the effects of polymer chain conformation on TC flow, which directly informs both the fluid elasticity and the shear thinning properties. Many studies until now have utilized non-ionic polymers like poly(ethylene oxide) (PEO), whose chain conformation will not change upon altering the solution ionic strength. Apostolakis *et al.* [39] and Hajizadeh and Larson [40] have explored the effects of stress-induced migration based on conformation tensor-based rheological models. Ionic or charged polymers, also known as polyelectrolytes, are typically water-soluble, and the hard charges from functional groups along the backbone make them superb materials for flocculation and coagulation processes in water treatment and paper-making [41,42]. At increased solution ionic strength, *[I]*, the electrostatic interactions between the like charges along the backbone are screened, which greatly reduces the electrostatic repulsion between the charged groups. The reduction in electrostatic repulsion also decreases the persistence length of a polymer chain, which allows for the polymer chains to adopt a more flexible, coiled conformation from an initially more stretched, expanded conformation [41,43,44]. In a series of studies by Metaxas *et al.* [45,46], the authors of the current work studied the flocculation and growth of bentonite clay-cationic polyacrylamide flocs in TC flows. However, the concentrations of polyelectrolyte present in these studies were not appreciable enough to study the effects of polyelectrolytes on TC flow.

This study addresses how flow states and transitions change due to the presence of a polyelectrolyte at varying ionic strengths in TC flow. More specifically, this study aims to better understand and characterize the flow states/instabilities and their critical transitions in Taylor-Couette flow due to the changes in polymer chain conformation of the polyelectrolyte because of changing solution ionic strength. To explore these variables, quasi-static ramping studies of the inner cylinder were performed with a commercial cationic polyacrylamide (CPAM) solution with varying amounts of NaCl to alter the solution ionic strength. Both stationary and rotating (co- and counter) outer cylinder studies were performed. Finally, flow state maps for each solution type were constructed to consolidate the varying flow states observed during these studies.

2. Materials and methods

2.1. Equipment

The Taylor-Couette cell used in this study consists of two independent concentric cylinders, with an anodized aluminum inner cylinder of diameter, $D_{in} = 13.54 \pm 0.01$ cm and a borosilicate glass outer cylinder of diameter, $D_{out} = 15.20 \pm 0.01$ cm. The annulus radial width between the cylinders *d* is 0.84 cm, and the annulus gap height *h* is 51 cm. The radius ratio η is 0.89, and the aspect ratio Γ is 60. The TC cell is placed into an acrylic box, which is filled with paraffin oil to match the refractive index of the glass outer cylinder and maintain the temperature of the system at approximately 22°C. Approximately 2 liters of fluid are required to fill the annulus between the cylinders. Additional design details and schematics about the TC cell can be found in earlier publications by Wilkinson *et al.* [47,48].

2.2. Test fluids and materials

The polyelectrolyte used in this study is a cationic polyacrylamide, CPAM, (FLOPAM FO 4190 SH, SNF Polydyne) with 10 mol% quaternary ammonium cation monomers along the backbone and an average molecular weight of 4-6 $\times$ 10^6 g mol^{-1}. A 0.2 wt.% stock polyelectrolyte solution was made by mixing the solid polymer pellets into distilled water for 30 min using a Jiffy mixer attachment. The polymer was kept in a refrigerator at 2°C overnight prior to use and was remade every 2

weeks per the manufacturer instructions. The distilled water for all experiments is from Premium Waters, Inc.

The stock 0.2 wt% polyelectrolyte solution was removed from the refrigerator and allowed to warm to room temperature (22°C) prior to use. A 1:10 dilution of the stock solution was made with distilled water for a final polyelectrolyte concentration of 0.02 wt% and was mixed with 25 mg l^{-1} Iriodin paint particles for flow visualization using a VELP Scientifica JTL4 flocculator for 30 min at 300 RPM. The concentration of the final solution ($c \sim 2 \times 10^{-4}$ g/cm^3) is below the overlap concentration for FLOPAM FO 4190 SH for the highest ionic strength solution ($c^* \sim 2.70 \times 10^{-4}$ g/cm^3), but slightly higher than lowest ionic strength solution ($c^* \sim 1.09 \times 10^{-4}$ g/cm^3).

The overlap concentrations and persistence lengths for the polymer solutions were approximated based on the inverse of intrinsic viscosities as a function of ionic strength from a study by Walldal and Åkerman [43], due to limitations in measuring the radius of gyration (R_g) for charged polymers using traditional static light scattering methods. Walldal and Åkerman [43] used a similar cationic polyacrylamide with a molecular weight that falls in the range of the CPAM used in the present study, therefore the approximations calculated here are reasonable. The radii of gyration (R_g) were calculated from the intrinsic viscosity, and the persistence length was then estimated from R_g. The persistence length observed an approximate dependence on ionic strength, *[I]*, of $[I]^{-0.5}$, varying from approximately 90 nm to 10 nm from ionic strengths of 0 to 50 mM. This demonstrates the more coiled nature of polymer chains at higher ionic strengths.

The ionic strength of the solution was changed by adding NaCl (Fisher Scientific) during the mixing process. Four different ionic strengths, *[I]*, of 0 mM, 1.3 mM, 10 mM, and 100 mM of polyelectrolyte solutions with measured densities of 0.996 ± 0.001 g ml^{-1}, 0.995 ± 0.001 g ml^{-1}, 0.996 ± 0.002 g ml^{-1}, and 0.999 ± 0.001 g ml^{-1}, respectively, were used in this study. Note that there technically is a non-zero solution ionic strength even at $[I] = 0$ mM due to the presence of the charged polyelectrolyte in solution. For the purposes of this study, ionic strength refers to added ionic strength from the addition of NaCl to solution. After 30 min of mixing, the solution was transferred to the annulus of the TC cell using a tube and valve attached to the bottom of the cell. For the Newtonian ramp experiments, a 33 wt% glycerol (Fisher Scientific) in distilled water solution was used with a density of 1.080 g ml^{-1}.

2.3. Rheological characterization

Steady shear rheology of the 0.02 wt% polyelectrolyte solution containing the 25 mg l^{-1} Iriodin at the four different ionic strengths listed above was measured on a TA Instruments AR-G2 rheometer using a cup and bob geometry (rotor o.d. 14 mm, rotor height 42 mm, cup i.d. 15 mm, and gap height 5 mm) at 22°C. The shear viscosity was measured after the torque signal reached equilibrium for shear rates, $\dot{\gamma}$, ranging from 1 s^{-1} to 300 s^{-1}. A power law (Eq. 3) can be fit to the portion of the shear viscosity, η_s, where there is a linear torque signal to obtain the flow behavior index, n, and the flow consistency index, K, as shown in Fig. S1. The flow behavior index increased from 0.678 ± 0.003 at $[I] = 0$ mM, 0.832 ± 0.005 at $[I] = 1.3$mM, and 0.968 ± 0.002 at $[I] = 10$mM, indicating that the solutions approached Newtonian-like behavior with increasing ionic strength. At $[I] = 100$mM, shear-thinning is not observed, and viscosity is independent of shear rate ($n = 1$).

$$\eta_s = K\dot{\gamma}^{n-1} \tag{3}$$

The fitted values for n and K, along with the reduced χ^2 and R^2 for the power law relationship and the range of shear rates over which the fit was performed, are given in Fig. S1 and Table S1. The torque signal is also provided to show which ranges of shear rates were excluded from the fit. At too low of shear rates, the viscosity data can appear higher than at higher shear rates and be misinterpreted as shear thinning when the increase is actually a result of low torque limit effects. At too high of shear rates, the viscosity data can also appear higher than at lower shear rates and be misinterpreted as shear thickening when the increase is actually a result of secondary flow effects [49].

The extensional relaxation time was measured using a HAAKE Capillary Breakup Extensional Rheometer (CaBER). For all experiments, 6 mm diameter steel plates were used with a 50 ms linear strike time. The solutions were loaded between the two plates at an initial separation distance of 3 mm and were allowed to equilibrate for 10 s. The plates were separated to a final height between 8 and 9 mm to impart a step strain on the fluid. Once the plates stopped moving, the fluid flows to form a self-thinning filament due to a balance between viscoelastic and capillary stresses. The midpoint of the fluid filament diameter is recorded over time until the filament breaks, and the results are shown in Fig. S2(a). The extensional relaxation time can be calculated using an elasto-capillary balance (Eq. 4) of the self-similar filament thinning process, where $D_{mid}(t)$ is the midpoint diameter of the filament as a function of time, D_0 is the initial filament diameter, G is the elastic modulus of the polymer, σ is the surface tension of the solution, t is time, and λ_E is the extensional relaxation time [50]. The product in front of the exponent is typically treated as a fitting constant. These results are shown in Fig. S2 (b) and Table S1, where the extensional relaxation time decreases with increasing solution ionic strength. The relaxation time is used to calculate solution elasticity, as mentioned previously in Section 1.2.

$$\frac{D_{mid}(t)}{D_0} = \left(\frac{GD_0}{4\sigma}\right)^{1/3} exp(-t/3\lambda_E) \tag{4}$$

2.4. System control

Both the inner and the outer cylinder can be independently rotated by separate stepper motors (Applied Motion Products HT34-497 2 phase stepper motor with a STAC5-S-E120 controller). Each motor has a 7:1 gear reducer (Applied Motion Products 34VL007) for balance of inertial motion between the cylinder and the motor. There is an additional speed reduction because of the different sizes of pulleys used on motor and the cylinder of 1:0.643. Each motor is controlled by an individual controller using text commands from LabVIEW. A Basler Ace camera (1280 × 1024, 60 Hz max) with a Tamron 25mm c-mount lens was used to capture movies of the ramping experiments. To illuminate the cylinder in a uniform fashion, an LED light strip (Metaphase 19" Exo2 Light) was axially aligned with the cell to provide a view of the θ-z plane. The LED light source provides flicker free lighting to eliminate additional noise in the Fourier transform frequency domains.

The acceleration ramp rate used in this study was non-dimensionalized by the viscous time scale, τ, where $\tau = t/(d^2/\nu)$, and can be expressed as $\frac{\partial Re_{in}}{\partial \tau} = \frac{\partial \Omega_{in}}{\partial t}\frac{r_{in}d^3}{\nu^2}$. The ramp rate at which the inner cylinder can be accelerated affects the formation and stabilization of flow states. For this study, the non-dimensional ramp rate was kept below 0.68, established by Dutcher and Muller [9] as the critical rate for quasi-static ramps. Due to quasi-static conditions, critical conditions for the flow state bifurcation do not change below this threshold for the ramp rate. It should be noted that for the non-Newtonian solutions, the kinematic viscosity depends on shear rate, and a dynamic ramp control (described below in Section 2.5) was used to maintain a constant $\frac{\partial Re_{in}}{\partial \tau}$ and, when applicable, a constant Re_{out} during the experiment.

2.5. Experimental procedure

To perform the ramp experiments, the annulus was filled with a solution of choice (33 wt% glycerol in water for the Newtonian solution or one of the four polyelectrolyte solutions at varying ionic strengths for the non-Newtonian solutions). Before commencing the ramp protocol, vortex dislocations were carefully removed following a previously established protocol [9]. Briefly, the inner cylinder speed was increased to a higher value and subsequently decreased to a lower value before the

start of the ramp experiments to ensure repeatability of the flow structure generated. A LabVIEW code was used to ramp the inner cylinder from a stationary position (Re_{in}= 0) while the outer cylinder was kept at a fixed Re_{out} (-100, 0, or 100). Since the polyelectrolyte solutions are non-Newtonian, their viscosities are not constant with shear rate. A Carreau regression model (Eq. 5) was used to calculate the effective viscosity by calculating a shear rate from a given motor speed and the functional form derived from steady shear rheology data to obtain an accurate value of Re_{in} during the ramp experiments. The Carreau model (Eq. 5) calculates an effective solution viscosity η_{eff} more accurately over

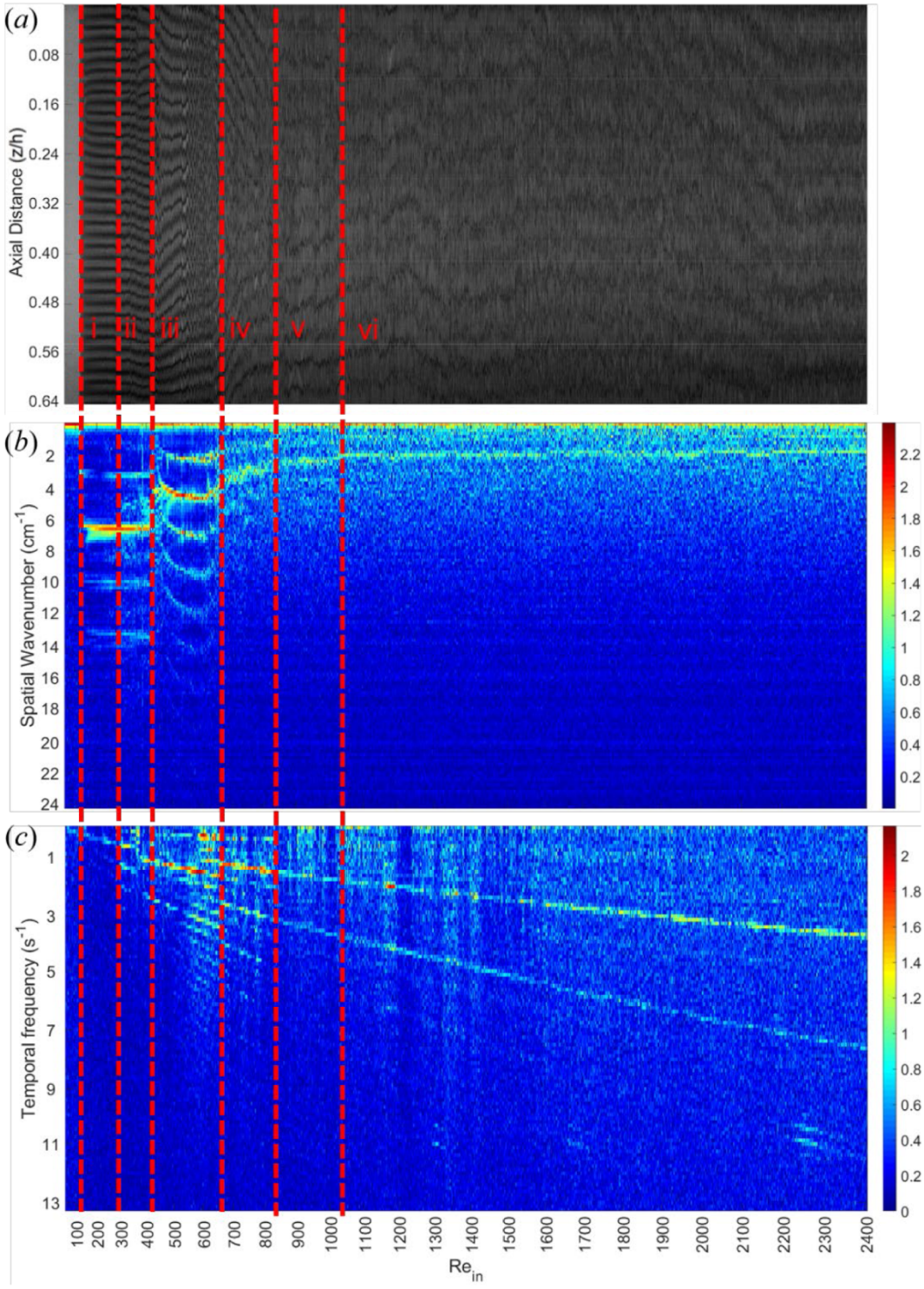

Fig. 1. (a) Space-time plot (Alternating light and dark bands represent the vortices and the space between them, respectively. The axial distance between vortices is non-dimensionalized by the height of the annulus) and corresponding Fourier plots in (b) space and (c) time for cationic polyacrylamide solutions with an ionic strength of 0 mM and stationary outer cylinder $Re_{out} = 0$. The color bars on the right-hand side of the contour plots indicate intensity. The flow transitions have been marked with the dotted red lines at the following inner cylinder Reynolds numbers: i) $Re_{in} = 128$, Taylor vortex flow, ii) $Re_{in} = 293$, wavy vortex flow, iii) $Re_{in} = 430$, modulated wavy vortex flow, iv) $Re_{in} = 638$ elongated jellyfish wavy vortex flow, and v) $Re_{in} = 817$, turbulent elongated jellyfish wavy vortex flow, and vi) $Re_{in} = 1022$, viscoelastic chaotic flow. Similar plots for the other solutions and other outer cylinder rotations can be found in Figs. S3 – S13 in the Supplementary Materials.

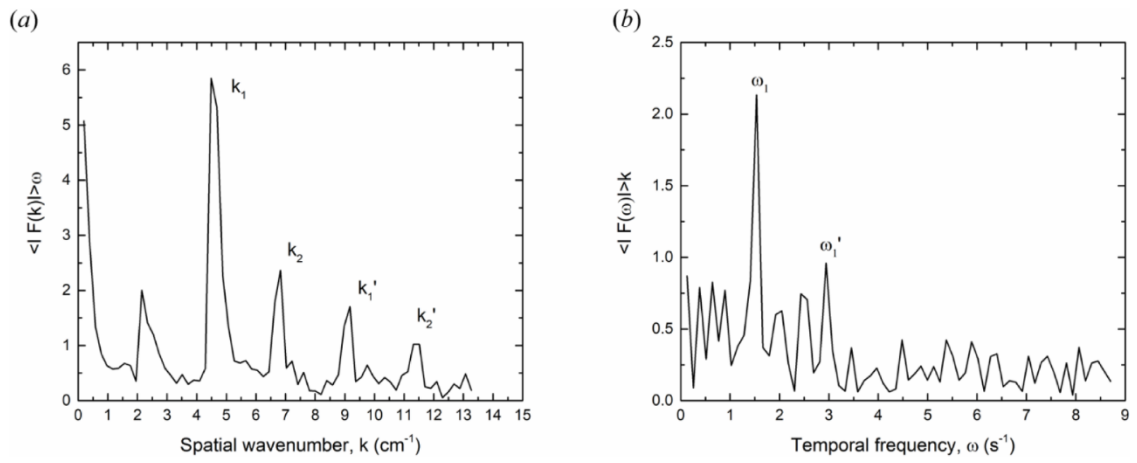

Fig. 2. (a) $<|F(k)|>_\omega$ is the absolute value of the spatial Fourier transform frequency magnitude averaged across all temporal frequencies, and (b) $<|F(\omega)|>_k$ is the absolute value of the temporal Fourier transform frequency magnitude averaged across all spatial frequencies. Both plots are at $Re_{in} = 505$, modulated wavy vortex flow state for cationic polyacrylamide solutions with an ionic strength of 0 mM and stationary outer cylinder. The labeled peaks in each plot represent the dominant frequencies at this specified Re_{in}. Note that k_1' is a harmonic to k_1, and ω_1' is a harmonic to ω_1.

a broader range of shear rates than the simple power-law expression (Eq. 3) used earlier to characterize the degree of shear-thinning of the solution. The Carreau model (Eq. 5) also considers additional variables: η_∞ is the viscosity at infinite shear rate, η_0 is the viscosity at zero shear rate, and λ is the shear relaxation time. The fit parameters are given in Table S1. Each ramp experiment took several hours to complete, ranging from 4-6 hrs. Once an experiment was completed, the video was processed, and the data were analyzed using a custom MATLAB script.

$$\eta_{eff}(\dot{\gamma}) = \eta_\infty + (\eta_0 - \eta_\infty)\left[1 + (\lambda\dot{\gamma})^2\right]^{\frac{n-1}{2}} \quad (5)$$

2.6. Image analysis

A space-time plot can be made by combining a single line of pixels oriented axially along the cylinder from each frame, as demonstrated by Dutcher and Muller [9] and Wilkinson and Dutcher [47], which is shown in Fig. 1(*a*). A Fourier transform was performed on the space-time plot to determine the spatial and temporal properties of the vortices as shown in Fig. 1(*b*) and (*c*), respectively, across the range of Re_{in} used in the study. The flow transitions are marked by the vertical, dashed red lines in the plot. To construct a 2D power spectrum, a 2D Fourier transform was applied to the space-time image. The 2D spectrum is then averaged spatially ($<|F(\omega)|>_k$) or temporally ($<|F(k)|>_\omega$) to analyze the frequency and size of the vortex structures, respectively, which are shown in Fig. 2. The dominant frequencies and their harmonics are visible in these plots, which aid in the characterization of the vortex structure and size. Similarly, the space time plots for all solutions with outer cylinder rotations of $Re_{out} = 100$ (co-rotation) and $Re_{out} = -100$ (counter-rotation) were analyzed, and the flow state transitions were mapped accordingly and can be seen in supplementary Figs. S3-S13. Based on the observed flow states and transitions, the following results are presented in the next section.

3. Results and discussion

3.1. Overview

This study aims to examine the effects of polymer chain

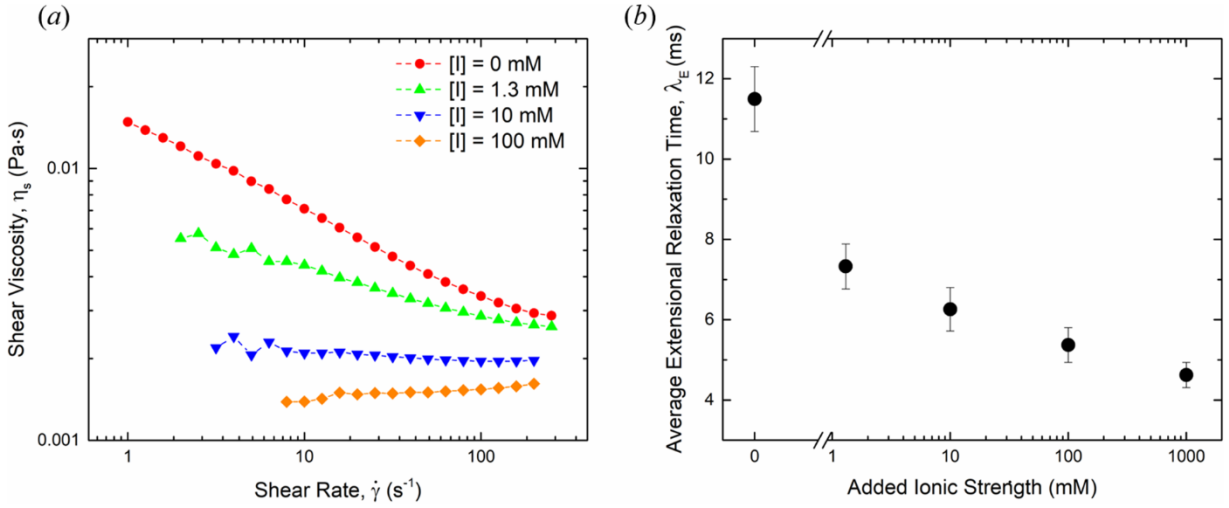

Fig. 3. (a) Steady shear viscosity as a function of shear rate for each solution used in the Taylor-Couette ramp studies. The data shown here are within a shear rate range that avoids artifacts due to low torque limit effects at lower shear rates and secondary flow effects at higher shear rates. The full data set including results at low and high shear rates is shown in Fig. S1. (b) Average extensional relaxation times as a function of ionic strength as determined from Capillary Breakup Extensional Rheometry (CaBER) using Eq. 4. The extensional relaxation times were used to calculate the elasticity, *El*, of each solution as shown in Fig. S2. Note that there technically is a non-zero solution ionic strength even at $[I] = 0$ mM due to the presence of the charged polyelectrolyte in solution. For the purposes of this study, ionic strength refers to added ionic strength from the addition of NaCl to the solutions.

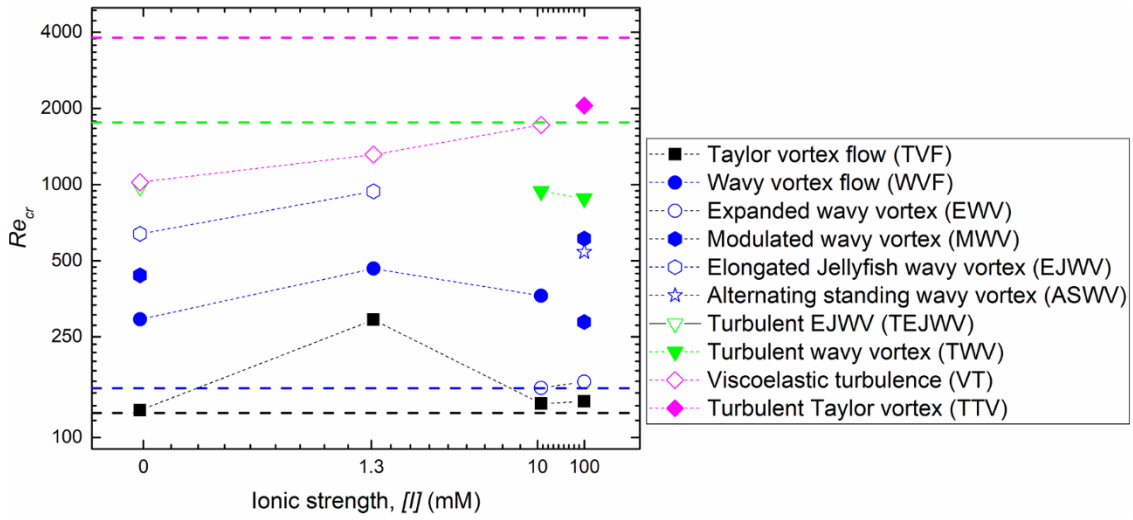

Fig. 4. Critical Reynolds number (Re_{cr}) for the onset of a flow state transition as a function of ionic strength. As the ionic strength increases, the flow behavior index, n, for the polyelectrolyte solutions also increases and approaches 1. Horizontal dashed lines correspond to Re_{cr} values for the Newtonian case. All experiments shown in this plot were performed with a stationary outer cylinder ($Re_{out} = 0$).

conformation on the flow dynamics observed in the Taylor-Couette system. The change in ionic strength results in change in equilibrium polymer chain conformation, leading to different rheological responses. The steady shear rheology traces of CPAM at various solution ionic strengths show that the polymer approaches Newtonian-like behavior as the ionic strength increases, as shown in Fig. 3(*a*). Both the degree of shear-thinning (parameterization by the flow behavior index, n) and the shear viscosity decrease with increasing ionic strength. The transition to Newtonian-like behavior with increased ionic strength can also be viewed by examining elasticity, *El*, for each solution in Fig. S2(*b*), where the elasticity, *El*, decreases as *[I]* increases. The elasticity was calculated using the extensional relaxation times determined by CaBER measurements, which are depicted in Fig. 3*(b),* and show a decrease in extensional viscosity with ionic strength. For the solution with *[I]* = 0 mM, the most elastic solution of the four non-Newtonian solution considered here, the elasticity reduces sharply with an increase in shear rate at the lower shear rate range, which corresponds to a change in flow behavior. The suppression of both the shear thinning behavior (n approaching 1) and the decrease in the elasticity are attributed to a decrease in persistence length and a conformation change of the cationic polyacrylamide from expanded to coiled [51]. Charge screening of the positive charges along the backbone results in the polyelectrolyte transitioning from a more expanded, stretched conformation at the lowest ionic strength (*[I]* = 0 mM) to a more coil-like, flexible conformation at the highest ionic strength (*[I]* = 100mM) [43]. This change in behavior has consequences for flow-state transitions and the emergence of new flow states, which are detailed in the following sections.

Sections 3.2 and 3.3 focus on flow states observed when keeping the outer cylinder stationary ($Re_{out} = 0$), while Section 3.4 focuses on the effects of co- and counter-rotation of the outer cylinder on flow instabilities. The full set of critical Reynolds number (Re_{cr}) for the onset of each new flow state are given for Re_{out} = -100, 0, and 100 in Table S2. Generally, there appears to be a delay in Re_{cr} for lower order laminar transitions in all non-Newtonian cases compared to the Newtonian case. The magnitude of delay for the second transition was much higher compared to the first transition. While the lower order transitions (*e.g.,*

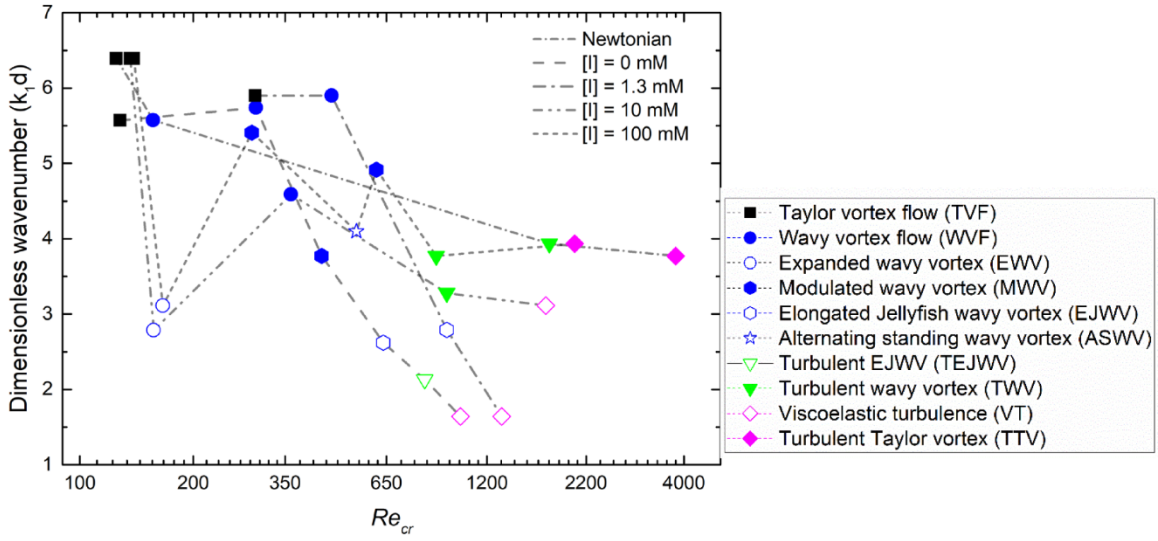

Fig. 5. Dimensionless spatial wavenumber, k_1d, is presented here as a function of Re_{cr} at the critical transition points for the Newtonian solution and the non-Newtonian solutions at varying ionic strengths. The lines connecting the critical transitions are to guide the eye; detailed evolution of the spatial frequency profile can be observed in Fig. 1b (*[I]* = 0 mM), Fig. S5 (*[I]* = 1.3 mM), Fig. S8 (*[I]* = 10 mM), and Fig. S11 (*[I]* = 100mM). All experiments shown were collected with a stationary outer cylinder ($Re_{out} = 0$).

TVF and WVF) were delayed, the higher order, chaotic and turbulence-dominated transitions (*e.g.,* TWV and TTV) occurred earlier compared to the Newtonian case. These findings are summarized in Fig. 4 for $Re_{out} = 0$, where the critical transitions points have been plotted as a function of the ionic strength, *[I]*. The horizontal lines correspond to the flow transition for the Newtonian case and can be used as a reference to see the difference in suppression or enhancement of the flow instability for the non-Newtonian cases. Critical flow transition onsets for co- and counter-rotation are shown in Figs. S14 and S15.

In addition to modifying the critical transition point, newer flow states were also observed as the polymer conformation changes, particularly for the more expanded conformations found at lower ionic strengths. The lower order transitions for the lower ionic strength solutions and most of the transitions for the higher ionic strength solutions displayed inertially-driven flow instabilities, while the higher order transitions for the lower ionic strength solutions displayed non-Newtonian flow instabilities. These flow states will be discussed in detail in the following sections.

For all flow states, the spatial wavenumber and temporal frequency at any point in flow are obtained from the respective frequency maps as discussed in Section 2.6. A general feature found in the flow behavior of the non-Newtonian solutions is that there appears to be critical *Re* values where the size of the vortices shrinks (wavenumber increases) or grows (wavenumber decreases) depending on the ionic strength. The early rapid decrease in the vortex size is especially apparent for the higher ionic strength solutions, while the later rapid vortex growth is especially apparent for the lower ionic strength solutions as seen in Fig. 5. This later point of rapid growth of the vortex, discussed in Section 3.3, coincides with the point after the steep change in the elasticity of the lower ionic strength solutions (*[I]* = 0, 1.3 mM) as shown in Fig. S2(*b*).

3.2. Laminar transitions

3.2.1. First transition – stationary vortices

Taylor vortex flow (TVF, Fig. S16) was the first flow state observed for all solutions, with some variation in size of the vortices for lower ionic strength solutions *[I]* = 0, 1.3 mM, as seen in Fig. 5. The spatial frequency maps (Fig. 5) reveal that the spatial wavenumber for higher ionic strength, flexible polymer conformation solutions matches closely to the Newtonian case and are larger compared to the lower ionic strength cases. Taylor vortices for the lower ionic strength solutions (*i.e. [I]* = 0, 1.3 mM) have larger vortex sizes (smaller wavenumbers) compared to the higher ionic strength solutions (*i.e. [I]* = 10, 100 mM) due to the expanded conformation of the polymer (larger degree of shear thinning and higher elasticity), as shown by Fig. 3 and Fig. S2(b). This effect can be explained with the help of 'rod climbing' or 'Weissenberg effect', which is well known in literature [52]. It observes the migration of polymer chains towards the center of the cylinder in a curvilinear flow, a volume force develops, which acts in the direction of curvature known as 'hoop stress' for viscoelastic fluids due to normal stress differences. Grossman and Steinberg [32] explain the formation of toroidal vortices based on the difference in hoop stress near the end and the middle. The hoop stress difference will be the largest for lower ionic strength solutions (*[I]* = 0, 1.3 mM) due to expanded polymer conformation compared to other cases, which leads to formation of slightly larger Taylor vortices. On the other hand, similarity in the vortex sizes at moderate and higher ionic strength solutions, where the polymer chain is in a more coiled conformation, can be attributed to the overall lower elasticity and suppression of shear thinning due to coiling, thus mimicking the behavior of the Newtonian solution (Table S1). Finally, the critical transition point (Re_{cr}) for the first transition is delayed for all the non-Newtonian solutions compared to the Re_{cr} of the first transition for the Newtonian solution, as shown in Fig. 4. However, there is no clear trend of the delay in Re_{cr} with polymer conformation.

3.2.2. Subsequent transitions – regular, expanded, and modulated waves

The second transition observed was wavy vortex flow (Fig. 6) for *[I]* = 0 mM and 1.3 mM, at a significantly suppressed Re_{cr}, and what we are referring to as expanded wavy vortex flow (EWV) for the *[I]* = 10 mM and *[I]* = 100 mM solutions (Fig. 7). The Newtonian-like WVF state observed for the lower ionic strength solutions has one characteristic temporal frequency in addition to one characteristic spatial frequency. The size of the WVF vortices is approximately the same as the previous TVF transition. The wavy transitions for the higher ionic strength solutions show different behavior from both the lower ionic strength solutions and Newtonian solutions. Shortly after the TVF transition for *[I]* = 10mM and *[I]* = 100 mM at $Re_{cr} = 136$ and 139, respectively, the flow pattern shifts to a wavy flow state at $Re_{cr} = 157$ and 166, respectively. In addition to the formation of waves, the new flow state, as observed in Fig. 7, is marked by larger vortex sizes (lower wavenumber, Fig. 5), which are almost double the size of the vortices in TVF. We therefore name this new flow state expanded wavy vortex flow (EWV). This effect can be attributed to the flexible, coiled conformation of polymer chains at these higher ionic strength conditions. At lower shear rates for these values of Re_{in}, Smith *et al.* [53] describes that the polymer chains will favor the tumbling state instead of a more stretched state. Another study

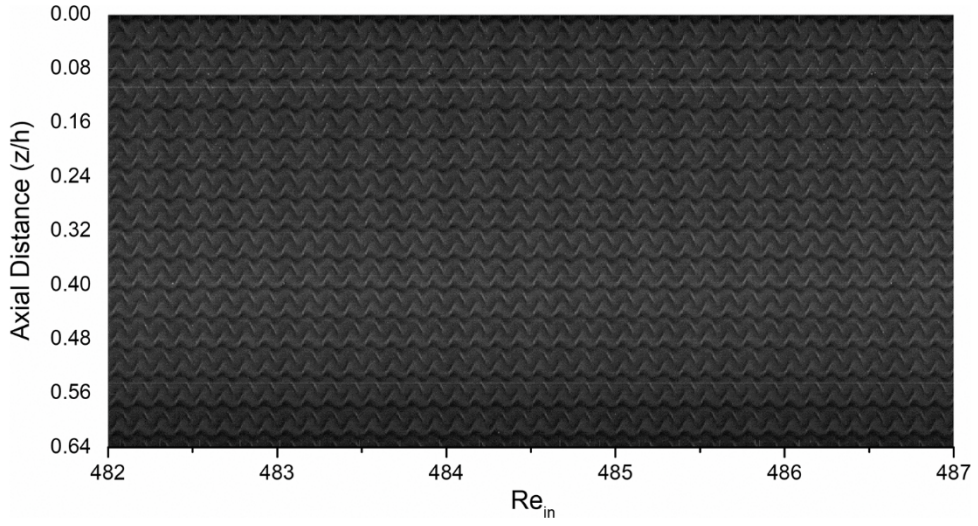

Fig. 6. Representative example of space-time plot for wavy vortex flow (WVF) at *[I]* = 0 mM. WVF is characterized by presence of wave like nature of the vortices. The grey bands represent the waving vortices, which is the result of a temporal frequency in the flow.

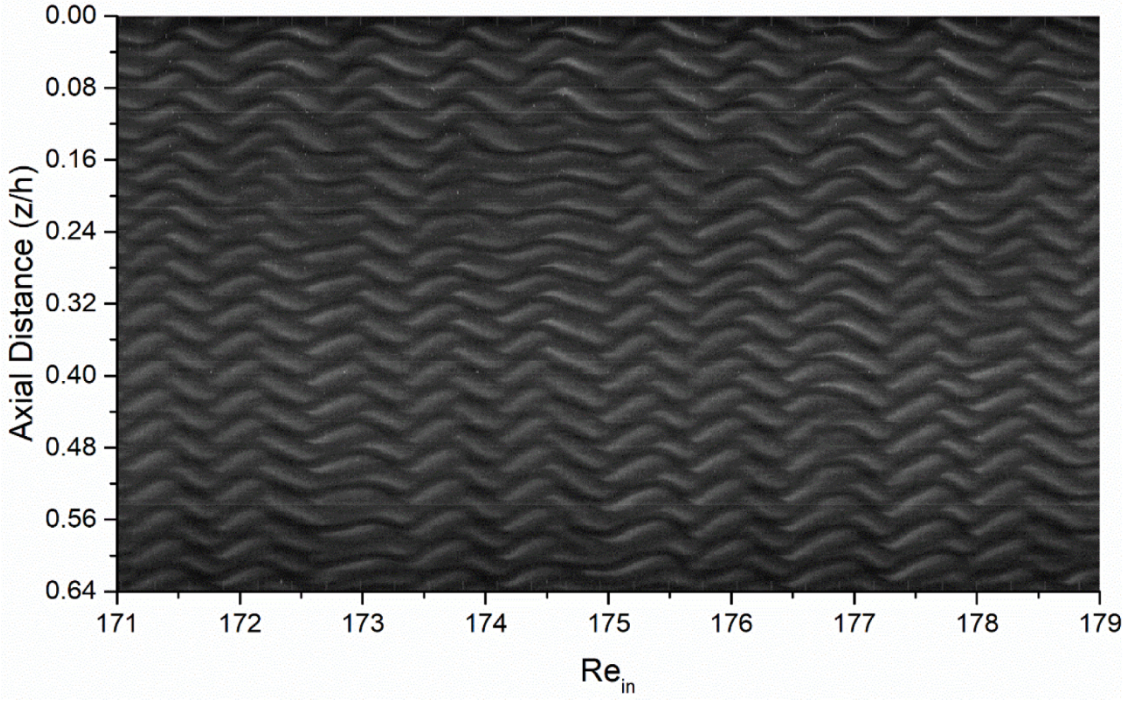

Fig. 7. Representative example of a space-time plot for expanded wavy vortex flow (EWV) at *[I]* = 100 mM. EWV is characterized by lager size of waving vortices. This flow state is an intermediate state for higher ionic strength (*[I]* = 10 mM and *[I]* =100 mM) polymer solutions.

by Soares *et al.* [54] found that flexible polymers can be source of smaller elasto-inertial instabilities at smaller *Re*, which might have attenuated the WVF to an expanded form.

Subsequent transitions that emerged were either modulated wavy vortex flow (MWV) (*[I]* = 0mM and *[I]* = 100mM) or WVF (*[I]* = 10 mM), which corresponds to the change in frequency of the wavy vortex flow. The critical transition point (Re_{cr}) for these wavy states when compared to the Newtonian solution for all polymer solutions are significantly delayed, as seen in Fig. 4. The delay in transition for WVF and MWV was more pronounced compared to the delay for the TVF transition when comparing to the Newtonian flow state. In addition, the Re_{cr} is higher for lower ionic strength solutions compared to higher ionic strength solutions. The higher transition Re_{cr} for lower ionic strength solutions can be attributed to the stabilizing and drag reducing properties due to the higher elasticity of stretched polymer solutions, which is a well-known effect [13,21].

The evolution of the spatial wavenumber (vortex size) is worth noting. The initial sharp decrease in spatial wavenumber (rapid vortex growth) for the higher ionic strength polymer solutions when transitioning to EWV from TVF was followed by rapid increase (vortices shrink) to WVF or MWV as the shear rate increased. Both lower ionic strength solutions (*[I]* = 0, 1.3 mM) with expanded conformation maintained the vortex size for WVF transition from previous flow state (TVF).

For the MWV transition from WVF, the drop in spatial wavenumber (vortex growth) for the lowest ionic strength solution (*[I]* = 0 mM) is much larger than other solutions as the polymer chains are in most stretched/expanded conformation. It is important to note here that polymer chains in this expanded form exhibit the highest degree of shear thinning and elasticity compared to other solutions. Due to this reason the polymer chains begin to be more readily shear thin at this point in the ramping for *[I]* = 0 mM, while the chains in the other solutions are not as affected. In other words, rapid vortex growth is observed (wavenumber decreases) for MWV as seen in Fig. 5. This point coincides with the change in elasticity curve in Fig. S2(*b*). However, no new flow state was observed for this point in the flow despite the change in vortex sizes.

When the flow transitions from EWV to WVF (*[I]* = 10 mM) and to modulated wavy vortex flow MWV (*[I]* = 100mM), the wavenumber increases (vortices shrink), but to a value lower than the initial TVF state. For further transitions, the flow states for higher ionic strength solutions have a more gradual decrease in wavenumber, where the vortex size for the *[I]* = 100 mM solution is similar to the Newtonian case. The smallest vortex size growth was observed for this solution as it has the most coiled conformation, resulting in the low elasticity and shear thinning.

3.2.3. *Alternating standing and elongated jellyfish waves*

In addition to the EWV state discussed in the previous sub-section, two other new non-Newtonian flow states were observed with increasing Re_{in}, including alternating standing wavy vortex flow (ASWV) and elongated jellyfish wavy vortex flow (EJWV). ASWV is a weak intermediate flow state observed for a short duration for the solution at *[I]* = 100 mM. This rather interesting intermediate flow state occurs for a short time between Re_{cr} = 545 and Re_{cr} = 600. Two different sizes of vortices are present next to each other in an alternating fashion as shown in Fig. 8, and this pattern is present throughout the length of the TC cell, similar to a vertical standing wave.

The ASWV state was only observed with the highest ionic solution (*[I]* = 100 mM). The emergence of this flow state can be explained in a similar way as before (Section 3.2.2), as the polymer chains are in most coiled/flexible conformation compared to other solutions. The flow state seems like a superimposition of EWV and WVF, where the relatively higher shear rate at this point in ramping compared to that of EWV results in both stretching of polymer chains along with tumbling, leading to the formation to local instabilities resulting in superimposition of two flow conditions. Because the flow state is unstable under these conditions, this effect lasts for a relatively short period of time. After ASWV, which occurred for a short time, the flow transitions back to uniform Newtonian-like WVF with similar spatial and temporal frequencies, which was present before the ASWV state.

For solutions containing polymer chains with more expanded/

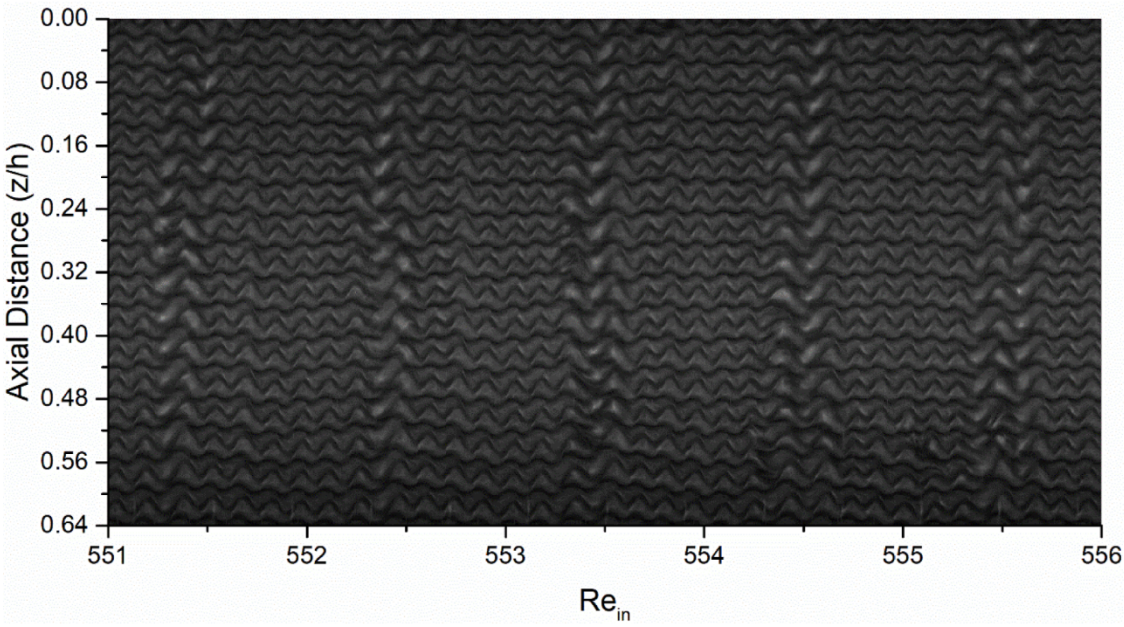

Fig. 8. Representative example of a space-time plot for alternating standing wavy vortex flow (ASWV) for the *[I]* = 100 mM solution. Alternating bands of different vortex sizes (*i.e.,* two distinct spatial frequencies) can be observed. There seems to be a superposition of two different flow conditions.

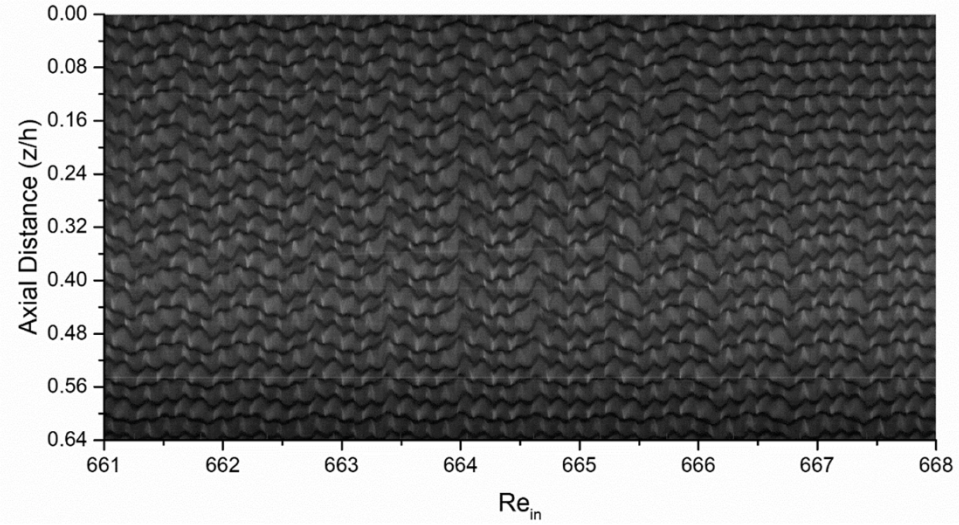

Fig. 9. Representative example of a space-time plot for elongated jellyfish wavy vortex flow (EJWV) at *[I]* = 0 mM. The vortices exhibit a distinct structure similar to a jellyfish, with a larger "head" connected to a "tail" shape, while waving simultaneously. This was observed for lower ionic strength solutions (*i.e.*, more expanded polymer conformations).

stretched forms (*[I]*=0, 1.3 mM), the higher order flow transitions occur via a centrally induced distortion, which eventually grows outwards from the center of the TC cell toward the top and bottom ends. The first instance of this was observed for *[I]* = 0 mM solution. Here, a new flow state is observed in which a pair of adjacent vortices behave in such a way that if one vortex grows, the other shrinks in size and vice versa, while the size of the pair of vortices remains almost constant. Also, the pair of vortices are waving at certain temporal frequency. where the vortices form a shape consisting of a larger-sized "head," followed by a narrow "tail-like" shape, resembling a jellyfish as shown in Fig. 9. There also appears to be a periodicity in change in size of vortex (spatial wavenumber). This new flow state is named as elongated jellyfish wavy vortex flow (EJWV). The EJWV flow state was observed for the *[I]* = 1.3 mM solution as well, but the critical transition point (Re_{cr} = 940) was delayed compared to the *[I]* = 0 mM case (Re_{cr} = 638). The elasticity response to shearing is similar for (*[I]* = 0, 1.3 mM) as seen in Fig. S2(*b*), where both have a steep reduction in elasticity at the beginning and then asymptote to a relatively constant value. The only difference is that the solution with *[I]* = 0 mM is more shear thinning than the *[I]* = 1.3 mM solution as it takes a higher shear rate to align the polymer chains with the flow to promote shear thinning. This might be the reason for similar but delayed flow behavior for *[I]* = 1.3mM when compared to *[I]* = 0 mM.

As expected, there was a further reduction in spatial wavenumber (vortex growth) for the EJWV from the previous wavy states. As the vortex size growth was much more rapid for expanded polymer solutions than the coiled polymer solutions. The vortices grew the most in the *[I]* = 1.3 mM solution, with the wavenumber dropping almost to half (vortex size doubling) of its value from the wavenumber of the previous state. The point where the wavenumber drops coincides with the change

in elasticity as shown in Fig. S2(*b*) as described above.

3.3. Turbulent transitions

3.3.1. Newtonian-like turbulence states

As with Newtonian flows, turbulent wavy and turbulent stationary vortices (*e.g.,* coherently wavy, or stationary vortices with small-sized eddies within each toroidal vortex) were observed at higher Re_{in}. However, the critical transitions points (Re_{cr}) for these states were much lower than those of the Newtonian solution. In addition, as ionic strength decreased (expanded polymer chain conformation), the turbulent states became less Newtonian-like, with new flow states emerging for the lower ionic strengths. The highest ionic strength ($[I] = 100$mM) case showed the smallest growth in vortex size. Therefore, with increasing coiling in polymer chains due to increasing ionic strength, vortex growth decreased. Temporal frequencies generally increased with Re_{in} for all polymer solutions.

The highest ionic strength case $[I] = 100$ mM exhibited turbulent wavy vortex flow (TWV) and turbulent Taylor vortex flow (TTV), where the latter flow state lost its characteristic temporal frequencies. Both were similar in behavior to the Newtonian solution. The spatial wavenumbers of the $[I] = 100$ mM and Newtonian solutions are both similar in value. Overall, the higher ionic strength solutions behaved more closely to the Newtonian solution, except for the turbulent transitions occurring at a much lower critical Reynolds numbers for the polymer solution. The TWV transition occurs at $Re_{cr} = 881$ for $[I] = 100$ mM (compared to $Re_{cr} = 1758$ for the Newtonian fluid) and the TTV transition occurs at $Re_{cr} = 2053$ for $[I] = 100$ mM (compared to $Re_{cr} = 3800$ for the Newtonian fluid) as seen in Fig. 4.

3.3.2. Non-Newtonian turbulent states

Like earlier results, the lower ionic strength solutions (expanded conformation) exhibit non-Newtonian flow behavior due to higher elasticity at the expanded conformations. The lowest ionic strength solution ($[I] = 0$ mM) was to the first polyelectrolyte solution to transition to a turbulent state. The elongated jellyfish waves transition to the turbulent EJWV (TEJWV) flow state at $Re_{cr} = 881$. The TEJWV flow retains the basic features of EJWV, but the effect of turbulence on the vortices is clearly marked by the emergence of intermittent turbulent spots destabilizing the flow, making vortices distorted and their structure is randomly disrupted as shown in Fig. 10. Viscoelastic turbulence (VT) is the final flow state observed for $[I] = 0$ mM and $[I] = 1.3$ mM solutions. The polymer solution at $[I] = 1.3$ mM skips the TEJWV flow state and directly transitions to VT.

For the polymer solution at $[I] = 10$ mM, TWV flow was observed, but TTV flow was absent. Instead, the flow terminates at high Re_{in} (up to 1746) for our ramping range with a viscoelastic turbulent flow (VT), shown in Fig. 11. As explained earlier, with increasing ionic strength the polymer chain transitions from a more expanded/stretched to a more coiled/flexible conformation. So, for $[I] = 10$ mM the persistence length will be between that of $[I] = 1.3$mM and that of $[I] = 100$mM. At this ionic strength, the charges along the backbone are not fully screened, resulting in a conformation somewhere between expanded and coiled, leading to having some degree of shear thinning (Table S1). As stated by Ryder and Yeomans [55], the radius of gyration fluctuations in a shearing flow increase for coiled/flexible polyelectrolyte chains as the chains are able to expand and contract more freely. Therefore, a higher shear rate is required to keep the polymer chains stretched due to their coiled nature and lower relaxation times. Only when the chains are fully stretched out in the flow is it possible for them to shear thin and exhibit elasto-inertial effects, creating a viscoelastic turbulence flow state. The more expanded, stretched out polyelectrolyte chains more easily align along the flow direction and exhibit suppressed fluctuation in their radius of gyration, resulting in greater shear thinning, thus explaining the emergence of these viscoelastic effects much earlier in the ramping stage. This also explains much earlier (after WVF) deviation for the lower ionic strength solutions from Newtonian-like flow states, while it takes much longer for the intermediate case of $[I] = 10$ mM to do the

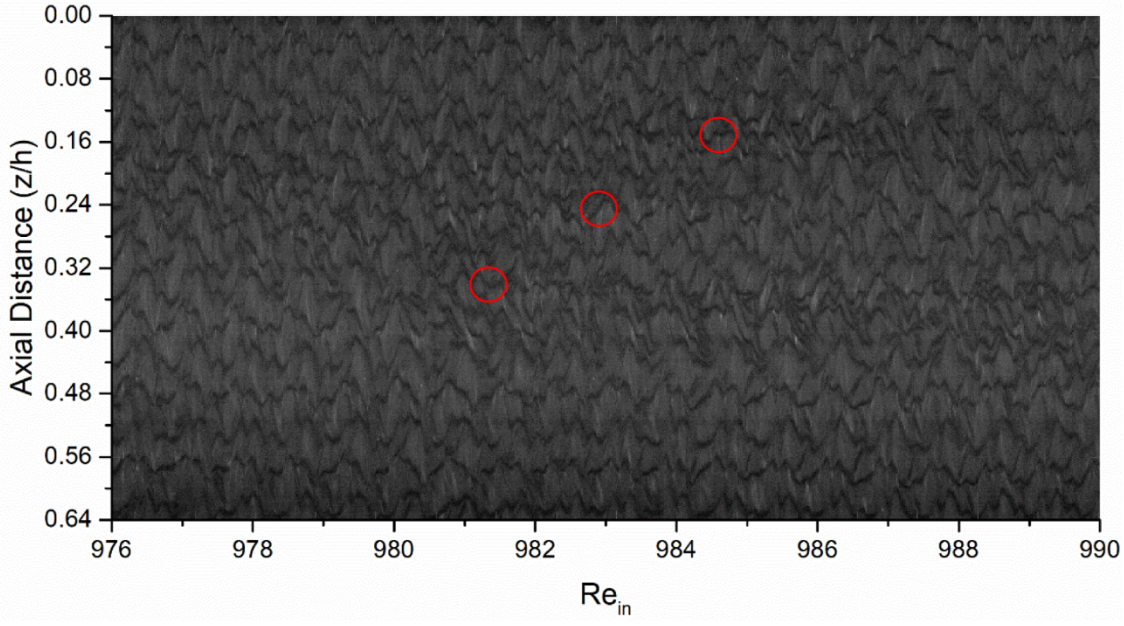

Fig. 10. Representative example of a space-time plot for turbulent elongated jellyfish wavy vortex flow (TEJWV) for $[I] = 0$ mM. Intermittent turbulent spots (INT) can be seen (marked by red circles) interspersed in EJWV flow.

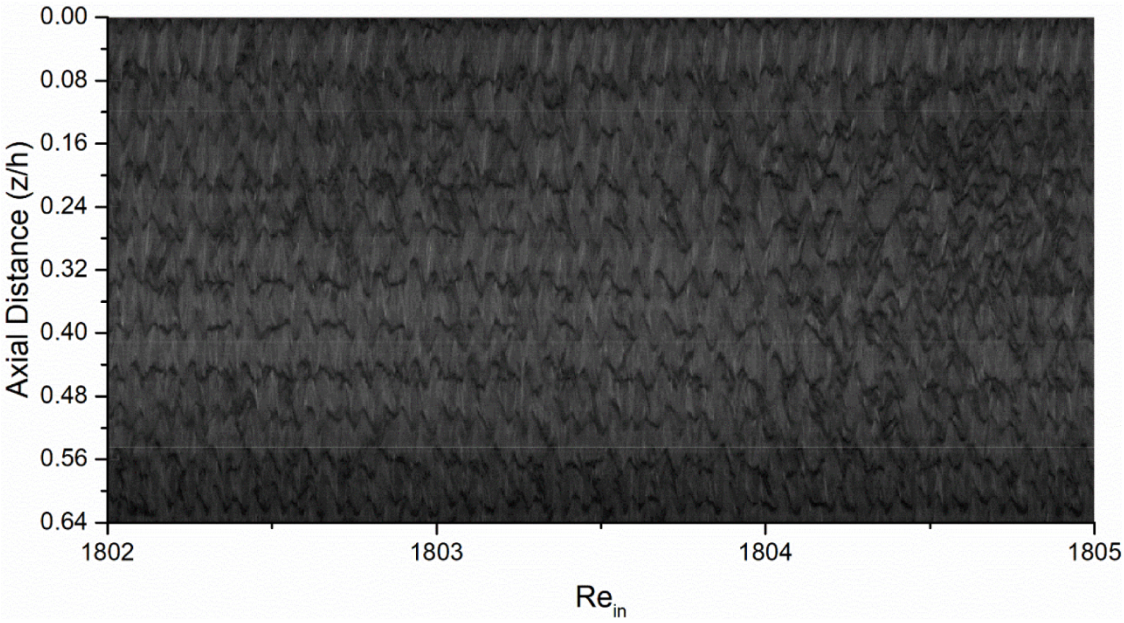

Fig. 11. Representative example of a space-time plot for elastically-driven viscoelastic turbulent flow (VT) at *[I]* = 0 mM. This flow state exhibits featureless turbulent flow, where the lighter and darker bands are chaotically mixed.

same.

3.4. Effects of co-and counter-rotation of the outer cylinder on flow transitions

3.4.1. Co-rotation

Co-rotation of the outer cylinder of a Taylor-Couette cell is known to have a stabilizing effect on symmetric flows and suppresses symmetry breaking of a given flow state [56]. Co-rotation can also provide an enhanced way to study the flow between the cylinders by stabilizing flow structures which were too weak to form or might not have appeared at all in the stationary outer cylinder case. For experiments conducted in this section of the study, the outer cylinder was rotated in the same angular direction as the inner cylinder with a constant $Re_{out} = 100$. As usual, the inner cylinder increased at the quasi-static ramp rate from stationary as described in Section 2.4.

As expected, in addition to flow states observed for stationary outer cylinder case, three weak, intermediate states were observed because of stabilization by co-rotation. The transitions follow similar paths from stationary vortices and waves to turbulent flows with several additions

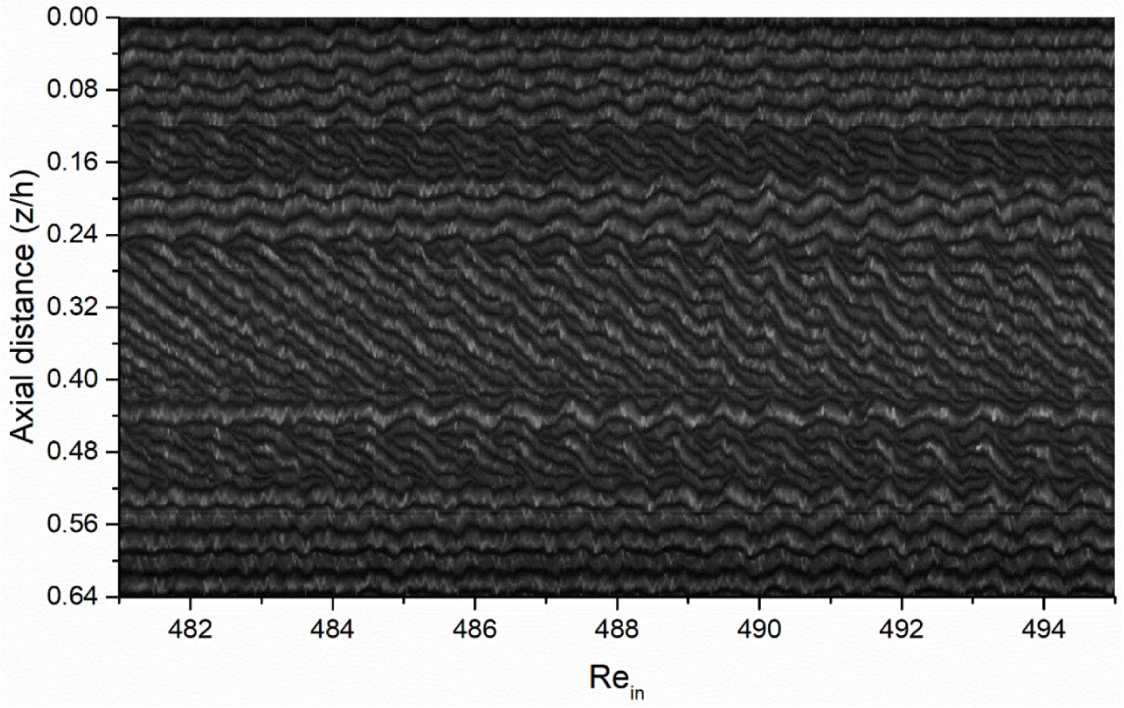

Fig. 12. Representative example of a space-time plot for helical wavy vortex flow (HWV) at *[I]* = 0 mM and $Re_{out} = 100$. The vortex flow transverses diagonally creating a helix like structure with a base wavy flow.

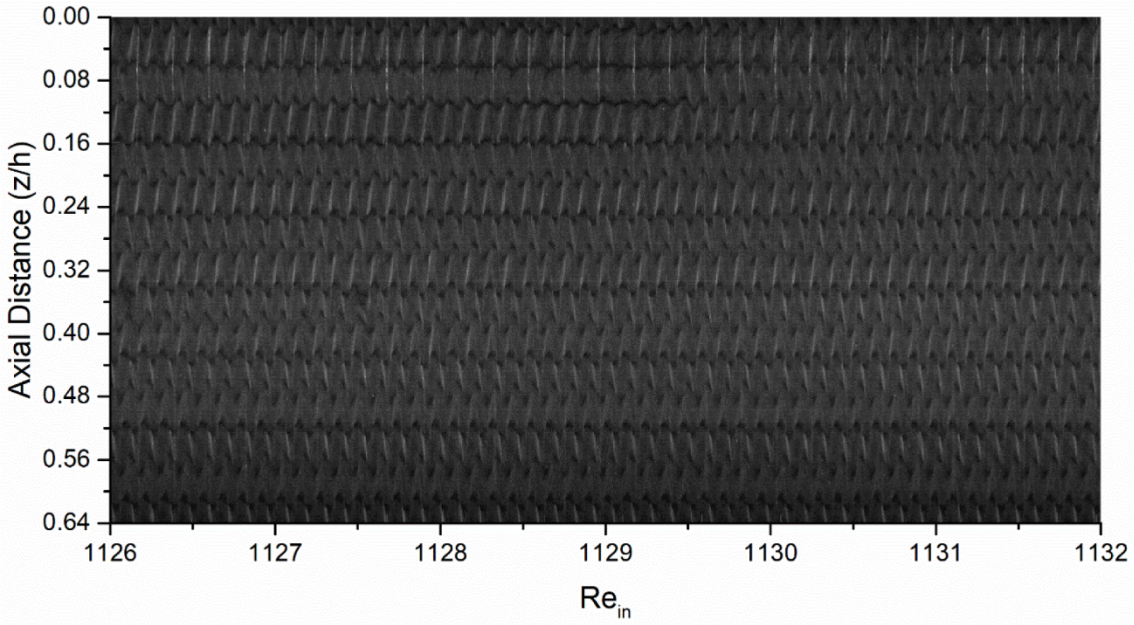

Fig. 13. Representative example of a space-time plot for over-expanded wavy vortex flow (OEWV) at *[I]* = 1.3 mM and Re_{out} = 100. The vortex size is the largest for all polymer solutions for a wavy flow almost twice the size of EWV.

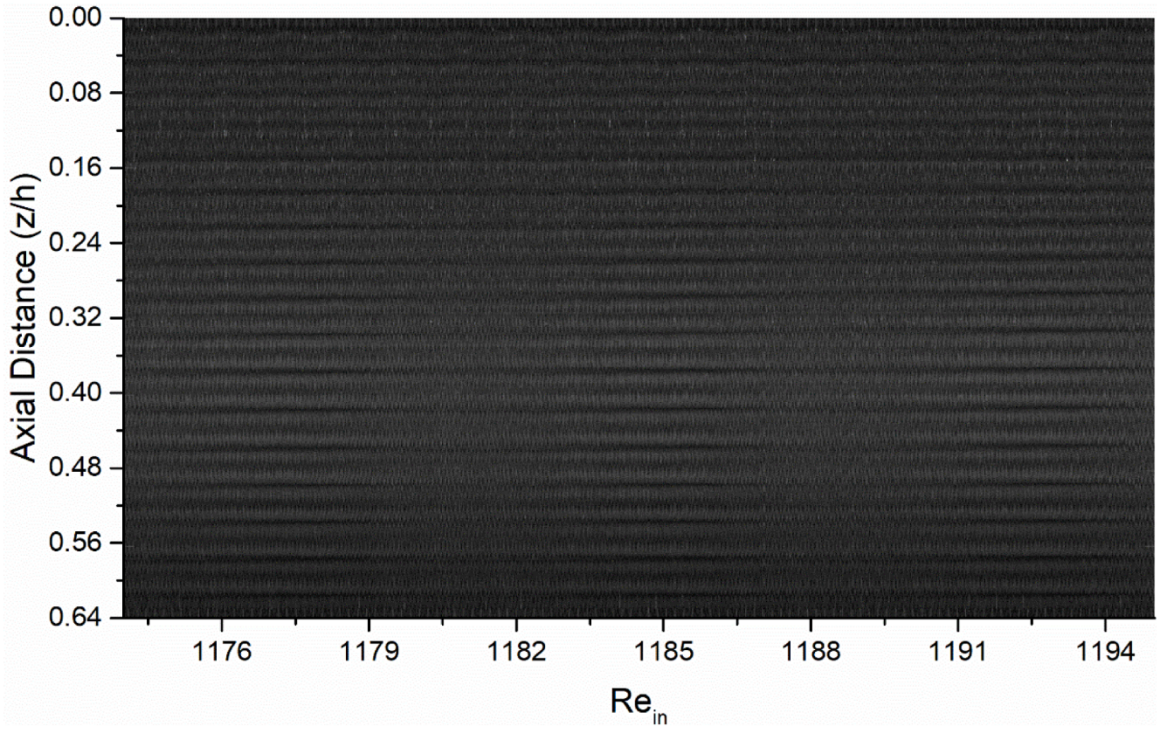

Fig. 14. Representative example of a space-time plot for longitudinal wavy vortex flow (LWV) at *[I]* = 100 mM and Re_{out} = 100. Alternating expansion and contraction of vortices can be observed, which results in alternating temporal frequencies at different locations in the flow.

as mentioned above. Starting with stationary vortices (TVF) for all polymer solutions except for *[I]* = 0 mM, which was succeeded by wavy vortex flow. The *[I]* = 0 mM solution commenced with smaller modulated wavy vortex flow, which was followed by a new helical wavy vortex flow state (HWV) as seen in Fig. 12. In HWV flow, some of the vortices intertwined to form a helix-like structure in the flow. This helix-like structure was observed before in the stationary outer cylinder case as a weak transition state from MWV to EJWV, but was too unstable to be sustained and captured. Co-rotation enabled these otherwise unstable flow states to be stabilized, captured, and characterized.

While the flow next transitions to MWV for *[I]* = 0 mM and *[I]* = 10 mM, the polymer solution at *[I]* = 1.3 mM transitions to expanded wavy vortex flow (EWV), which was previously seen for the higher ionic strength polymer solutions (*[I]* = 10 mM and *[I]* = 100 mM) in Fig. 7. The EWV flow for the *[I]* = 1.3 mM solution subsequently transitions to a new over-expanded wavy vortex flow (OEWV) observed in Fig. 13. The OEWV flow state is remarkably like the expanded wavy vortex flow, but the size of the vortices is almost double that of EWV, might be due to the

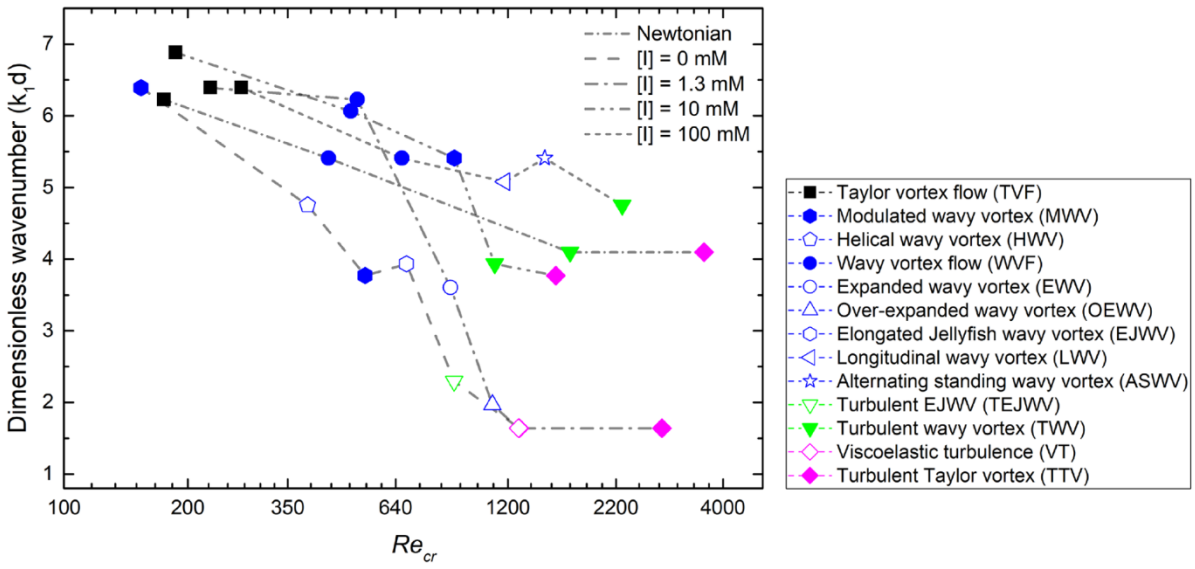

Fig. 15. Dimensionless spatial wavenumber, k_1d, is presented here as a function of Re_{cr} at the critical transition points for the Newtonian solution and the non-Newtonian solutions at varying ionic strengths. The lines connecting the critical transitions are to guide the eye; detailed evolution of the spatial frequency profile can be observed in Fig. S4 ($[I] = 0$ mM), Fig. S7 ($[I] = 1.3$ mM), Fig. S10 ($[I] = 10$ mM), and Fig. S13 ($[I] = 100$mM). All experiments shown were collected with a co-rotating outer cylinder ($Re_{out} = 100$). Overall, transitions are delayed for co-rotation of outer cylinder compared to the stationary case since the flow states are stabilized. The overall trends shown here are like those seen in the stationary outer cylinder case.

stabilization effect of co-rotation (Table S2). The $[I] = 10$ mM solution transitioned to the more traditional Newtonian turbulent wavy vortex flow. For the $[I] = 0$ mM solution, the EJWV were formed around the same critical Reynolds number as the stationary outer cylinder case. Unlike the stationary outer cylinder case ($Re_{out} = 0$), where EJWV flow was a weak stable flow state appearing for a smaller duration of time, EJWV was much more stabilized here and did not revert to WVF as it did for the $Re_{out} = 0$ case. Instead, it directly transitioned to the turbulent EJWV, as previously observed for $Re_{out} = 0$ (shown in Fig. 10). A new flow state was observed for the $[I] = 100$ mM solution case, where the flow transitioned from WVF to longitudinal wavy vortex flow (LWV). Like EJWV, which observed periodicity in spatial wavenumber. The unique feature of LWV flow was the presence of periodicity in temporal frequency, which can be seen as the alternating expansion and compression of a vertical band of vortices along the cell as shown in Fig. 14.

The LWV can be seen as a precursor to ASWV Flow (Fig. 8), which was the next transition for the $[I] = 100$ mM solution. Here, the expansions and compressions condensed into alternating standing waves of different frequencies. The LMV transition can only be captured due to the stabilization by co-rotation of the cylinders. This highlights the importance of co-rotation of cylinder in study of these weakly stable flow states and provide insight in formation of ASWV flow. The final transition for the lower ionic strength solutions ($[I] = 0$ mM and $[I] = 1.3$ mM) was to viscoelastic turbulence as observed before ($Re_{out} = 0$) which is shown in Fig. 11. For the higher ionic strength solutions, the $[I] = 10$mM solution followed similar Newtonian-like transitions to turbulent Taylor vortex flow, while the $[I] = 100$ mM solution transitioned to turbulent wavy vortex flow. The TWV for $[I] = 100$ mM solution is most likely capable of transition to turbulent Taylor vortex flow at even higher inner cylinder speeds, but due to the low solution viscosity and several other physical constraints prevented the experiment from running long enough.

The spatial wavenumber variation with critical Reynolds number follows a similar trend as the stationary outer cylinder case ($Re_{out} = 0$) for both higher and lower ionic strength solutions and can be seen in Fig. 15. Similar sharp drops in wavenumber were observed for lower ionic strength solutions (more expanded polymer chain conformations). The higher ionic strength solutions (more coiled polymer chain) behaved closer to Newtonian-like solutions as expected, which is in line with results obtained with the stationary outer cylinder. In general, the onset of the flow states was delayed compared to the stationary cylinder case as the flow states are stabilized due to co-rotation of the outer cylinder. This is visible in Fig. 15, where the curves are shifted to the right compared to their stationary counterparts.

3.4.2. Counter-rotation

Counter-rotation of the outer cylinder of the TC cell can have the exact opposite effect of co-rotation. That is, counter-rotation enhances breaking of the symmetric flow states and destabilizes them [56]. Like the co-rotation case, the outer cylinder was rotated at a fixed rate but in the opposite angular direction of the inner cylinder with a constant $Re_{out} = -100$. As expected, several of the flow states observed before were suppressed and others were distorted or destabilized due to the destabilization effects of counter-rotation of the cylinders.

While all the polymer solutions started with Taylor vortex flow, a reduction in vortex size was noticed with increasing ionic strength, with $[I] = 100$ mM having the smallest vortex size observed yet in all cylinder rotation cases. The follow up flow state to the stationary vortices was the introduction of waves for all polymer solutions with additional effects in some conditions. The flow transitioned to modulated wavy vortex flow for the lower ionic strength cases ($[I] = 0$ mM, 1.3 mM) whereas for higher ionic strength solutions, the flow transitioned to chaotic wavy vortex flows (CWVF) due to the combined effects of destabilization by counter-rotation and increased polymer chain flexibility. The flow did briefly transition to a familiar expanded wavy vortex flow (EWV) with increased vortex size (Table S2) before reverting to CWVF. The polymer solution at $[I] = 10$ mM matched closely with the stationary outer cylinder case, as the flow transitioned to the expanded wavy vortex flow (Fig. 7), which was succeeded by WVF. The only difference here was a slight delay in transition points for the flow states. Eventually, the flow did transition to CWVF after WVF as an effect of destabilization.

Following the path of the stationary outer cylinder case, the next wavy transition for $[I] = 0$ mM shows an early occurrence of EJWV for a short duration before becoming destabilized. However, EJWV does eventually destabilize due to the counter-rotation, which can be observed in Fig. 16 as random distortion to the jellyfish vortices starts appearing in the flow. It is worth noting that the flow is not turbulent at

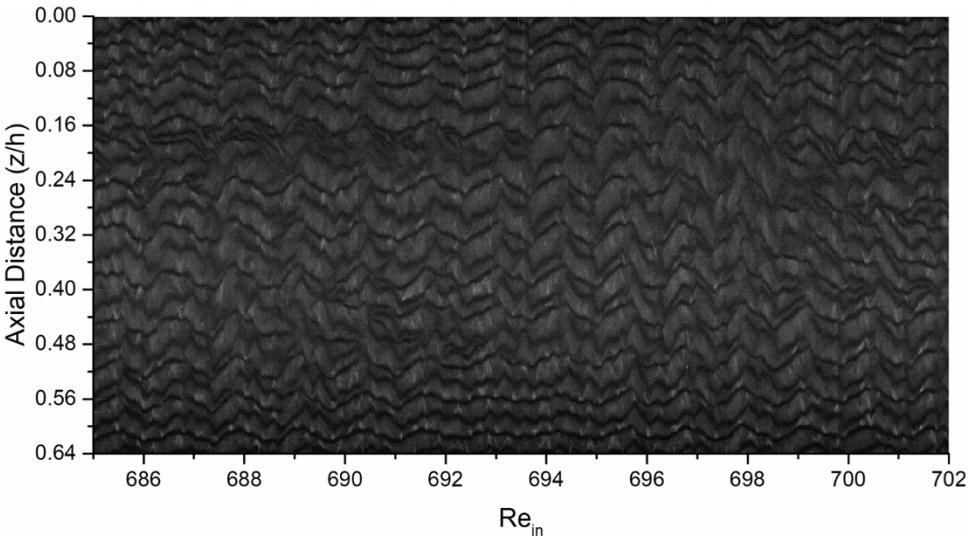

Fig. 16. Representative example of a space-time plot for distorted EJWV flow (DEJWV) at *[I]* = 0 mM and Re_{out} = -100. Counter-rotation of the outer cylinder destabilizes the flow and distorts the EJWV for the lower ionic strength solutions. The flow distortions can be seen at various location in the space-time plot.

this stage as the shear rate is comparatively low. This flow state is therefore appropriately named distorted EJWV (DEJWV) due to the presence of local instabilities.

Interestingly, for the *[I]* = 1.3 mM polymer solution, the flow skips the EJWV flow states and transitions directly to a distorted EJWV (Fig. 16). As the flow enters the turbulent regime for the final transitions, the distorted EJWV flow state transitions to the turbulent EJWV (TEWJV) (Fig. 10) for the *[I]* = 0 mM and *[I]* = 1.3 mM solution. The difference between the distorted EJWV state (Fig. 16) and the turbulent EJWV state (Fig. 10) is that the flow is still not turbulent in the case of DEJWV, and distortions in the flow were caused by the destabilizing effects of counter-rotation rather than turbulence *i.e.* only local instabilities were present in the flow instead of the whole flow being turbulent. For both the lower ionic strength solutions (*[I]* = 0 mM and *[I]* = 1.3 mM), the final transition is to viscoelastic turbulence. For the higher ionic strength solutions (*[I]* = 10 mM and *[I]* = 100 mM), the conventional transition from turbulent wavy vortex flow to turbulent Taylor vortex flow was present.

Fig. 17 provides a quantitative depiction of the vortex size behavior and stability of the flow states for counter-rotation of the outer cylinder. The higher ionic strength solutions start out with much smaller vortex sizes like the Newtonian solution. The same is not true for the lower ionic strength solutions, which have approximately the same size vortices as the stationary case. Like the stationary outer cylinder case, the vortex size rapidly grew for the lower ionic strength solutions. The delay for the occurrence of same flow state was reduced between the *[I]* = 0 mM and *[I]* = 1.3 mM solutions in the counter-rotation case, whereas it was enhanced by the co-rotation case. This is a clear indication of the flow stabilization and destabilization effects of the co-rotation and counter-rotation, respectively. For counter-rotation, the overall curve appears to be shifted to the left of the stationary outer cylinder case (Fig. 5), resulting in the early occurrences of the

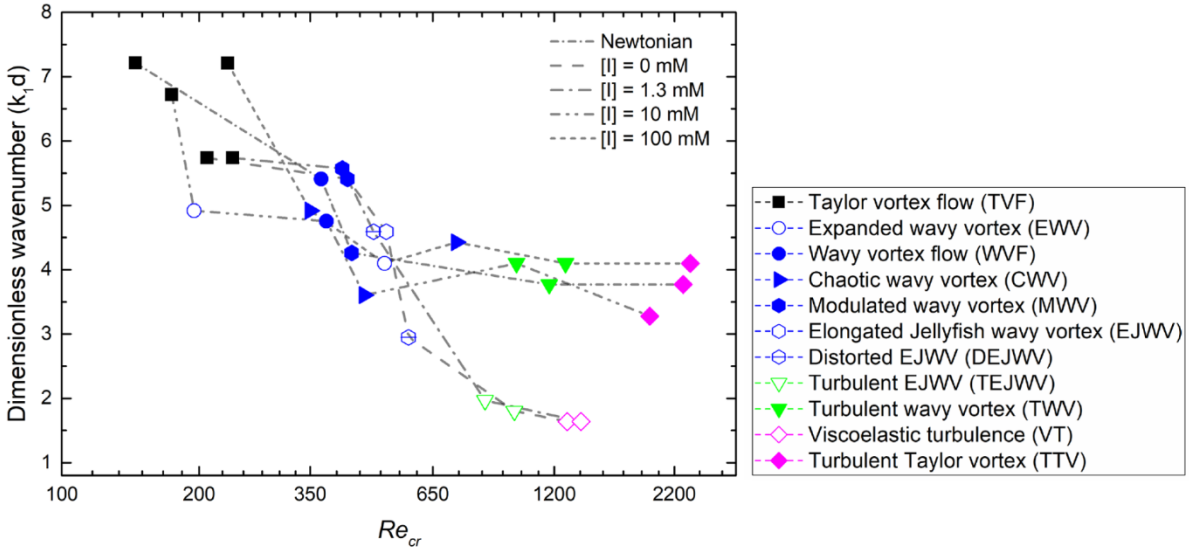

Fig. 17. Dimensionless spatial wavenumber, $k_1 d$, is presented here as a function of Re_{cr} at the critical transition points for the Newtonian solution and the non-Newtonian solutions at varying ionic strengths. The lines connecting the critical transitions are to guide the eye; detailed evolution of the spatial frequency profile can be observed in Fig. S3 (*[I]* = 0 mM), Fig. S6 (*[I]* = 1.3 mM), Fig. S9 (*[I]* = 10 mM), and Fig. S12 (*[I]* = 100mM). All experiments shown were collected with a counter-rotating outer cylinder (Re_{out} = -100). Overall, the transitions occur earlier than those of the stationary outer cylinder case. The overall trends are like those seen in co-rotation and with the stationary outer cylinder.

transitions. The important thing to note here is that most of the destabilized transitions were initiated by a distortion (locally present instabilities disrupting the flow) in or around the center of the TC cell that grew outwards toward the ends of the TC cell.

3.5. Flow state maps for non-Newtonian solutions

Flow state maps like those referenced at the beginning of the study for the Newtonian solutions as a function of both Re_{in} and Re_{out} can be generated from this study for the non-Newtonian solutions. Fig. 18 shows a total of four flow state maps, where each map corresponds to a solution ionic strength. The $[I] = 0$ mM solution deviated the most from Newtonian flow, with the appearance of new flow states including EJWV and viscoelastic turbulence. The $[I] = 1.3$ mM solution initially has Newtonian-like transitions but deviates at higher order transitions. The $[I] = 10$ mM solution was the closest to the Newtonian solution in terms of the shared flow states. The only exception is the appearance of EWV flow due to the increased flexibility of the polymer chains at this ionic strength. Finally, the $[I] = 100$ mM solution shows several new flow states such as ASWV and LWV that emerge due to the solution containing the most flexible polymer chains of all the polyelectrolyte solutions. Table 1 provides the summary of rheological properties as well as the flow states observed all four polymer solutions. Due to the nature of polymer solutions, the fluid properties change with shear rate in the experiment. Threfore, the values for lower shear rate (approaching zero shear) and a representative higher shear rate (160 s^{-1}) are provided for

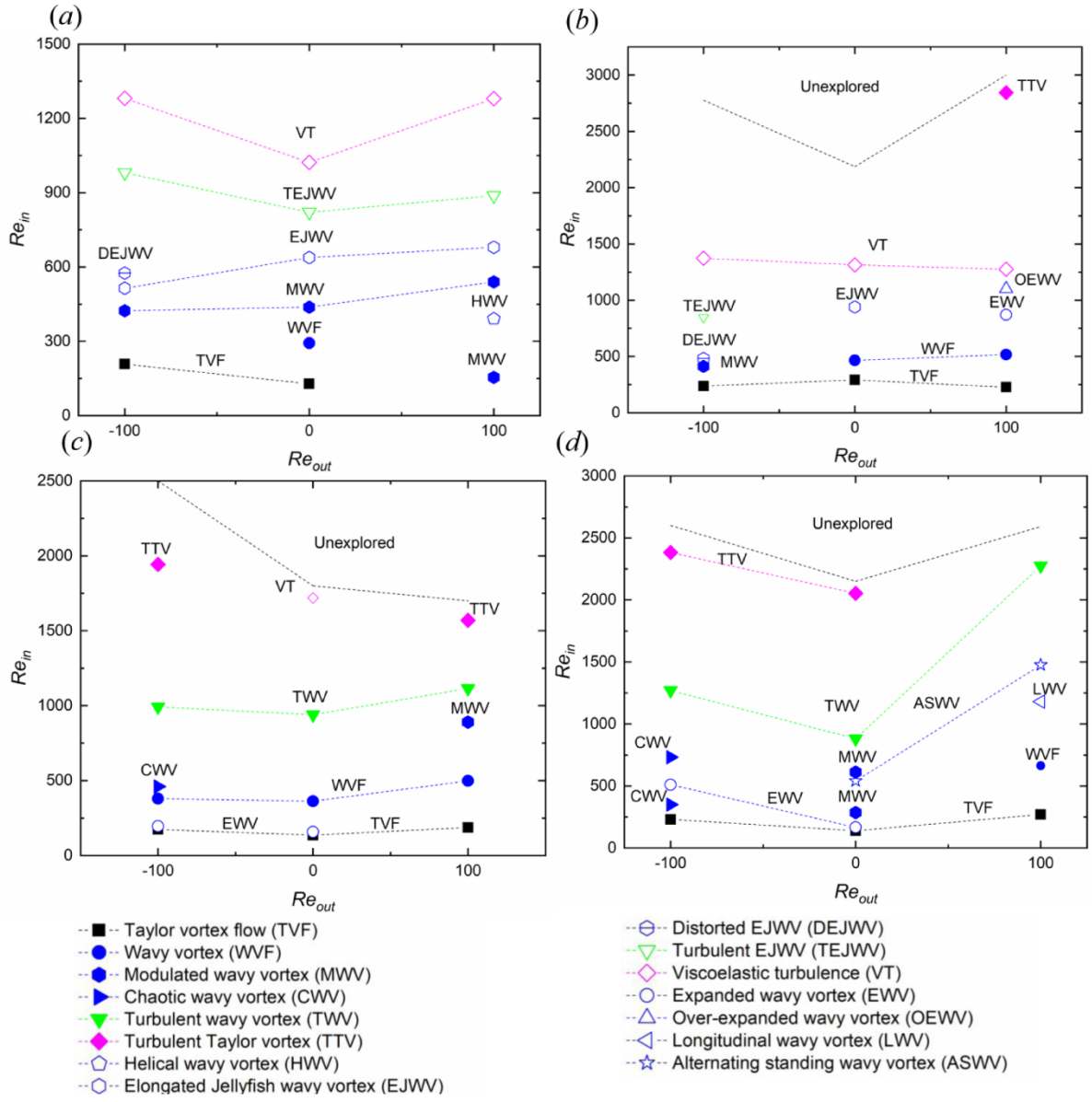

Fig. 18. Flow state maps as a function of Re_{in} and Re_{out} for polyelectrolyte solutions at ionic strengths of (a) $[I] = 0$ mM, (b) $[I] = 1.3$ mM, (c) $[I] = 10$ mM, and (d) $[I] = 100$ mM.

Table 1
Summary of flow transition sequences in Taylor–Couette flows.

Ionic strength [mM]	Viscosity ratio (η_p/η_s)	Elasticity (El)	Normal stress coefficient (Pa.s^2)	Viscosity ratio (η_p/η_s)	Elasticity (El)	Normal stress coefficient (Pa.s^2)	Transition sequence ($\uparrow Re_{in}$)	Re_{out}
Zero shear				Shear rate (160 s^{-1})				
0	14.96	2.48×10^{-3}	0.85	1.48	5.11×10^{-4}	3.39×10^{-5}	TVF↑MWVF↑EJWV↑DEJWV↑TEJWV↑VT	-100
							TVF↑WVF↑MWVF↑EJWV↑TEJWV↑VT	0
							MWV↑HWV↑MWV↑EJWV↑TEJWV↑VT	100
1.3	3.06	5.54×10^{-4}	0.83	1.24	2.90×10^{-4}	3.32×10^{-5}	TVF↑MWV↑DEJWV↑TEJWV↑VT	-100
							TVF↑WVF↑EJWV↑VT	0
							TVF↑WVF↑EWV↑OEWV↑VT↑TTV	100
10	1.32	2.40×10^{-4}	0.84	0.62	1.78×10^{-4}	3.34×10^{-5}	TVF↑EWV↑WVF↑CWV↑TWV↑TTV	-100
							TVF↑EWV↑WVF↑TWV↑VT	0
							TVF↑WVF↑MWV↑TWV↑TTV	100
100	0.76	1.62×10^{-4}	0.86	0.30	1.23×10^{-4}	3.43×10^{-5}	TVF↑CWV↑EWV↑CWV↑TWV↑TTV	-100
							TVF↑EWV↑MWV↑ASWV↑MWV↑TWV↑TTV	0
							TVF↑WVF↑LWV↑ASWV↑TWV	100

*Values are for 0.02 wt% cationic polyacrylamide with radius ratio = 0.89 and aspect ratio = 60.

comparison of flow conditions. It also includes the flow transition sequence for all polymer solutions at three different Re_{out}.

4. Conclusions

This study has investigated the effects of changing polymer chain conformation of a polyelectrolyte solution on flow states and transitions in a Taylor-Couette cell. The polymer chain conformation was controlled by varying the ionic strength of the solution, where at lower ionic strengths the polymer chains adopt a more expanded, stretched conformation while at higher ionic strengths the polymer chains adopt a more coiled, flexible conformation due to the charge screening on the backbone of the polymer chain. Prior studies have examined the effects of shear thinning and elasticity on TC flow, but the effects of changing polyelectrolyte chain conformation on flow transitions in Taylor Couette system have not been extensively studied before to the best of our knowledge. A well-defined ramping protocol combined with flow visualization has been used to identify and characterize the flow states.

At lower ionic strengths, the expanded polymer chain conformation allows the solution to have higher elasticity and a greater degree of shear thinning compared to higher ionic strength solutions. As a result, the flow states and critical transition points (Re_{cr}) were more affected by the elasto-inertial instabilities and ability of the solution to shear thin more readily. New flow states such EJWV flow, distorted and turbulent EJWV flow and HWV flow were observed as a result this. In terms of spatial wavenumber (vortex size change), the wavenumber decreased at more rapid rate compared to the higher ionic strength solutions, which represents the rapid increase in the size of the vortices due to the hoop stresses developed in the flow.

At higher ionic strengths, the flow behavior was markedly different than solutions at lower ionic strengths due to the more coiled conformation of the polyelectrolyte chains in solution. While most of the flow states observed for these solutions are closer to Newtonian-like flow states in terms of types of flow observed, the coiled, flexible nature of the polymer chain adds additional layer of complexity in the flow. Polymer chains tumble in addition to being stretched under shear, giving rise to local instabilities in the flow. Result of this can be seen as the emergence of new flow states, such as ASWV flow, LWV flow, EWV flow, and OEWV flow. As expected, the higher ionic strength solutions also closely follow the spatial wavenumber (vortex size) behavior of the Newtonian solutions. This is characterized by a gradual decrease in vortex size except for the formation of large wavy vortices (EWV and OEWV) during the intermediate transitions, where a dip in spatial wavenumber was observed. Flow states in higher ionic strength solutions are therefore affected more by the decreased persistence length of the polymer chains, resulting in the more flexible conformation and reduction of elasticity and shear thinning.

Additional effects with co- and counter-rotation were also explored in this study to the determine the effects of outer cylinder rotation on the stability of flow between the cylinders. Co-rotation was able to better stabilize weakly stable flow states, and stable flow states persisted for longer durations during the ramping protocol. Similarly, counter-rotation destabilized the flow states and suppressed the weakly stable flow states. When looking at the spatial wavenumber plots, stabilization and destabilization were clearly present visible for co-rotation and counter-rotation cases, respectively. For the co-rotation experiments, a relatively low slope for the wavenumber reduction was observed and the onset of flow states was delayed compared to the stationary and counter-rotation cases. For counter-rotation, the wavenumber curve is shifted to the left compared to the stationary case to mark the steep growth in vortex size due to increased stresses as an effect of counter-rotation.

Finally, flow maps were constructed from the ramping experiments to mark the types of flow states observed and the critical transition points relative to no, co-, and counter-rotation of the outer cylinder for each of the four different ionic strength solutions. This study hopefully provided a systematic approach to identify and characterize the flow states and understand effects of polymer chain conformation effects on TC flow, an area which was largely unexplored up to this point and encourages further exploration.

Declaration of Competing Interest

The authors report no conflict of interest.

Acknowledgments

Acknowledgment is made to the donors of the American Chemical Society Petroleum Research Fund for support of this research. This work was also partially supported by the National Science Foundation through the University of Minnesota MRSEC under Award Number DMR-1420013 and DMR-2011401. Part of this work was carried out in the College of Science and Engineering Polymer Characterization Facility, University of Minnesota, which has received capital equipment funding from the NSF through the UMN MRSEC program under Award

Number DMR-1420013. A.M. was supported through a National Science Foundation Graduate Research Fellowship.

Supplementary materials

Supplementary material associated with this article can be found, in the online version, at doi:10.1016/j.jnnfm.2021.104617.

References

[1] C.S. Dutcher, S..J. Muller, Explicit Analytic Formulas for Newtonian Taylor-Couette Primary Instabilities, Phys. Rev. E 75 (2007), 047301.
[2] R. Hollerbach, G. Rüdiger, New Type of Magnetorotational Instability in Cylindrical Taylor-Couette Flow, Phys. Rev. Lett. 95 (2005), 124501.
[3] G.I. Taylor, VIII, Stability of a Viscous Liquid Contained between Two Rotating Cylinders, Philos. Trans. R. Soc. London. Ser. A, Contain. Pap. a Math. or Phys. Character 223 (1923) 289–343.
[4] D. Coles, Transition in Circular Couette Flow, J. Fluid Mech 21 (1965) 385–425.
[5] H..A. Snyder, Waveforms in Rotating Couette Flow, Int. J. Non. Linear. Mech. 5 (1970) 659–685.
[6] T.J. Walsh, R..J. Donnelly, Taylor-Couette Flow with Periodically Corotated and Counterrotated Cylinders, Phys. Rev. Lett. 60 (1988) 700–703.
[7] C..A. Jones, The Transition to Wavy Taylor Vortices, J. Fluid Mech. 157 (1985) 135–162.
[8] C..D. Andereck, S.S. Liu, H..L. Swinney, Flow Regimes in a Circular Couette System with Independently Rotating Cylinders, J. Fluid Mech. 164 (1986) 155–183.
[9] C..S. Dutcher, S.J. Muller, Spatio-Temporal Mode Dynamics and Higher Order Transitions in High Aspect Ratio Newtonian Taylor-Couette Flows, J. Fluid Mech. 641 (2009) 85–113.
[10] C..D. Andereck, R. Dickman, H..L. Swinney, New Flows in a Circular Couette System with Co-Rotating Cylinders, Phys. Fluids 26 (1983) 1395–1401.
[11] M.A. Fardin, C. Perge, N. Taberlet, The Hydrogen Atom of Fluid Dynamics"- Introduction to the Taylor-Couette Flow for Soft Matter Scientists, Soft Matter 10 (2014) 3523–3535.
[12] N. Cagney, S. Balabani, Taylor-Couette Flow of Shear-Thinning Fluids, Phys. Fluids 31 (2019), 053102.
[13] O. Crumeyrolle, I. Mutabazi, M. Grisel, Experimental Study of Inertioelastic Couette-Taylor Instability Modes in Dilute and Semidilute Polymer Solutions, Phys. Fluids 14 (2002) 1681–1688.
[14] R.G. Larson, S.J. Muller, E.S..G. Shaqfeh, The Effect of Fluid Rheology on the Elastic Taylor-Couette Instability, J. Non-Newton. Fluid Mech. 51 (1994) 195–225.
[15] N. Ashrafi, Stability Analysis of Shear-Thinning Flow between Rotating Cylinders, Appl. Math. Model. 35 (2011) 4407–4423.
[16] T.J. Lockett, S..M. Richardson, W..J. Worraker, The Stability of Inelastic Non-Newtonian Fluids in Couette Flow between Concentric Cylinders: A Finite-Element Study, J. Non-Newton. Fluid Mech. 43 (1992) 165–177.
[17] S. Khali, R. Nebbali, D..E. Ameziani, K. Bouhadef, Numerical Investigation of Non-Newtonian Fluids in Annular Ducts with Finite Aspect Ratio Using Lattice Boltzmann Method, Phys. Rev. E 87 (2013) 53002.
[18] D..G. Thomas, B. Khomami, R. Sureshkumar, Nonlinear Dynamics of Viscoelastic Taylor-Couette Flow: Effect of Elasticity on Pattern Selection, Molecular Conformation and Drag, J. Fluid Mech. 620 (2009) 353–382.
[19] M.M. Denn, J.J. Roisman, Rotational Stability and Measurement of Normal Stress Functions in Dilute Polymer Solutions, AIChE J 15 (1969) 454–459.
[20] R.F. Ginn, M.M. Denn, Rotational Stability in Viscoelastic Liquids: Theory, AIChE J 15 (1969) 450–454.
[21] H. Rubin, C. Elata, Stability of Couette Flow of Dilute Polymer Solutions, Phys. Fluids 9 (1966) 1929–1933.
[22] N. Liu, B. Khomami, Elastically Induced Turbulence in Taylor-Couette Flow: Direct Numerical Simulation and Mechanistic Insight, J. Fluid Mech. 737 (2013) 4.
[23] M.V. Majji, S. Banerjee, J.F. Morris, Inertial Flow Transitions of a Suspension in Taylor-Couette Geometry, J. Fluid Mech. 835 (2018) 936–969.
[24] H. Mohammadigoushki, S.J. Muller, Inertio-Elastic Instability in Taylor-Couette Flow of a Model Wormlike Micellar System, J. Rheol. 61 (2017) 683–696.
[25] C. Perge, M.A. Fardin, S. Manneville, Inertio-Elastic Instability of Non Shear-Banding Wormlike Micelles, Soft Matter 10 (2014) 1450–1454.
[26] B.M. Baumert, S.J. Muller, Flow Visualization of the Elastic Taylor-Couette Instability in Boger Fluids, Rheol. Acta 34 (1995) 147–159.
[27] B..M. Baumert, S.J. Muller, Flow Regimes in Model Viscoelastic Fluids in a Circular Couette System with Independently Rotating Cylinders, Phys. Fluids 9 (1997) 566–586.
[28] B.M. Baumert, S.J. Muller, Axisymmetric and Non-Axisymmetric Elastic and Inertio-Elastic Instabilities in Taylor-Couette Flow, J. Non-Newton. Fluid Mech. 83 (1999) 33–69.
[29] C..S. Dutcher, S..J. Muller, Effects of Weak Elasticity on the Stability of High Reynolds Number Co- and Counter-Rotating Taylor-Couette Flows, J. Rheol. 55 (2011) 1271–1295.
[30] C.S. Dutcher, S.J. Muller, Effects of Moderate Elasticity on the Stability of Co- and Counter-Rotating Taylor–Couette Flows, J. Rheol. 57 (2013) 791–812.
[31] A. Groisman, V. Stelnberg, Elastic Turbulence in a Polymer Solution Flow, Nature 405 (2000) 53–55.
[32] A. Groisman, V. Steinberg, Elastic Turbulence in Curvilinear Flows of Polymer Solutions, New J. Phys. 6 (2004) 29.
[33] K. Arun Kumar, M.D. Graham, Buckling Instabilities in Models of Viscoelastic Free Surface Flows, J. Non-Newton. Fluid Mech. 89 (2000) 337–351.
[34] M.M. Cross, Relation between Viscoelasticity and Shear-Thinning Behaviour in Liquids, Rheol. Acta 18 (1979) 609–614.
[35] A. Groisman, V. Steinberg, Solitary Vortex Pairs in Viscoelastic Couette Flow, Phys. Rev. Lett. 78 (1997) 1460–1463.
[36] A. Groisman, V. Steinberg, Mechanism of Elastic Instability in Couette Flow of Polymer Solutions: Experiment, Phys. Fluids 10 (1998) 2451–2463.
[37] M. Lange, B. Eckhardt, Vortex Pairs in Viscoelastic Couette-Taylor Flow, Phys. Rev. E 64 (2001), 027301.
[38] R.G. Larson, E..S.G. Shaqfeh, D.S.J. Muller, A Purely Elastic Instability in Taylor-Couette Flow, J. Fluid Mech. 218 (1990) 573–800.
[39] M.V. Apostolakis, V..G. Mavrantzas, A.N. Beris, Stress Gradient-Induced Migration Effects in the Taylor-Couette Flow of a Dilute Polymer Solution, J. Non-Newton. Fluid Mech. 102 (2002) 409–445.
[40] E. Hajizadeh, R..G. Larson, Stress-Gradient-Induced Polymer Migration in Taylor-Couette Flow, Soft Matter 13 (2017) 5942–5949.
[41] B. Bolto, J. Gregory, Organic Polyelectrolytes in Water Treatment, Water Res 41 (2007) 2301–2324.
[42] I. Grillo, I. Morfin, J. Combet, Chain Conformation: a Key Parameter Driving Clustering or Dispersion in Polyelectrolyte – Colloid Systems, J. Colloid Interface Sci. 561 (2020) 426–438.
[43] C. Walldal, B. Åkerman, Effect of Ionic Strength on the Dynamic Mobility of Polyelectrolytes, Langmuir 15 (1999) 5237–5243.
[44] A.V. Walter, L.N. Jimenez, J. Dinic, V. Sharma, K.A. Erk, Effect of Salt Valency and Concentration on Shear and Extensional Rheology of Aqueous Polyelectrolyte Solutions for Enhanced Oil Recovery, Rheol. Acta 58 (2019) 145–157.
[45] A. Metaxas, N. Wilkinson, E. Raethke, C.S. Dutcher, In Situ Polymer Flocculation and Growth in Taylor-Couette Flows, Soft Matter 14 (2018) 8627–8635.
[46] A.E. Metaxas, V. Panwar, R.L. Olson, C.S. Dutcher, Ionic Strength and Polyelectrolyte Molecular Weight Effects on Floc Formation and Growth in Taylor-Couette Flows, Soft Matter 17 (2021) 1246–1257.
[47] N. Wilkinson, C.S. Dutcher, Taylor-Couette Flow with Radial Fluid Injection, Rev. Sci. Instrum. 88 (2017), 083904.
[48] N.A. Wilkinson, C.S. Dutcher, Axial Mixing and Vortex Stability to in Situ Radial Injection in Taylor-Couette Laminar and Turbulent Flows, J. Fluid Mech. 854 (2018) 324–347.
[49] R.H. Ewoldt, M.T. Johnston, L.M. Caretta, in Complex Fluids Biol. Syst, 2015, pp. 207–241 (Springer, New York, NY.
[50] S.L. Anna, G..H. McKinley, Elasto-Capillary Thinning and Breakup of Model Elastic Liquids, J. Rheol. 45 (2001) 115–138.
[51] E.D. Ruud, N..A. Wilkinson, C.S. Dutcher, Polymer and Particle Dynamics and Assembly in Varied Hydrodynamic Fields, Macromol. Chem. Phys. 217 (2016) 390–402.
[52] K. Weissenberg, A Continuum Theory of Rheological Phenomena, Nature 159 (1947) 310.
[53] D.E. Smith, H..P. Babcock, S. Chu, Single-Polymer Dynamics in Steady Shear Flow, Science 283 (1999) 1724–1727.
[54] E.J. Soares, I..M. Silva, R..M. Andrade, R.N. Siqueira, The Role Played by the Flexible Polymer Polyacrylamide (PAM) and the Rigid Polymer Xanthan Gum (XG) on Drag in Taylor–Couette Geometry: From Taylor's Vortexes to Fully Turbulent Flow, J. Brazilian Soc. Mech. Sci. Eng. 42 (2020) 392.
[55] J.F. Ryder, J.M. Yeomans, Shear Thinning in Dilute Polymer Solutions, J. Chem. Phys. 125 (2006), 194906.
[56] A. Schulz, G. Pfister, S.J. Tavener, The Effect of Outer Cylinder Rotation on Taylor-Couette Flow at Small Aspect Ratio, Phys. Fluids 15 (2003) 417–425.